Extending and Enhancing the MOSES Survey

MPhys Astrophysics

Louis Dabbs

Jeremiah Horrocks Institute
University of Central Lancashire

A thesis submitted in partial fulfilment for the requirements for the
degree of Master of Science (by Research)

September 2021

Declaration

Type of Award: Master of Science by research

School: School of Natural Sciences

I declare that while registered as a candidate for the research degree, I have not been a registered candidate or enrolled student for another award of the University or other academic or professional institution.

I declare that no material contained in the thesis has been used in any other submission for an academic award and is solely my own work.

No proof-reading service was used in the compilation of this thesis.

Louis Dabbs

September 2021

Abstract

This thesis outlines a project to enhance and extend the MOSES Survey undertaken at the MHT telescope by [Rambukwella-Gill, 2019]. Through improvements made to the reduction process, treatment of the world coordinate system (WCS), and method used to identify variables in the dataset, the number of variables identified increased from 719 in the first iteration of the survey [Rambukwella-Gill, 2019] to 1495 in the second despite applying a more restrictive magnitude range. In addition, Gaia EDR3 data has been combined with the MOSES data to create a HR-Diagram to aid in the classification of identified variables. Preliminary analysis was performed on a selection of the most variable stars identified, using the Gaia HR-Diagram to provide additional information to aid in the classifications suggested by light curves and periods of variability. We identified 1495 Variable stars. 7 were then analysed closely, and allowed us to classify a Cepheid, an LPV, an RV-Tauri star and three Eclipsing Binaries.

Contents

List of Figures

Acknowledgements

1 Introduction

This thesis describes the improvements made to the MOSES Project initiated by Amar Rambukwella-Gill in 2018. The MHT Optical Star and Exoplanet Survey (MOSES Project) is a stellar variability survey conducted using the Moses Holden Telescope (MHT) at Alston Observatory. Originally, this MSc project planned to take advantage of the six month observing season to obtain more observations, substantially increasing the time baseline. Unfortunately, due to a combination of weather, damage to the observatory's dome, and the ongoing COVID-19 pandemic, collection of new data was not possible. Fortunately, the data collected in the 2018 iteration proved sufficient to provide the basis of this thesis. The project's primary aim was the implementation of improvements to the data reduction process from the first iteration, and progression of the analysis into the variable stars the project identified.

Many ongoing surveys focus on the study of variability, the MOSES survey fits a niche between two of the most important, current surveys, the *Transiting Exoplanet Survey Satellite (TESS)* [TESS Team, 2014], and the *Zwicky Transient Facility (ZTF)* [Bellm et al., 2018]. The TESS survey has an observation window of 27.4 days per segment of the sky, with each segment being a 24°x 96° patch of the sky [TESS Team, 2014]. After this time period, the telescope moves to a different segment to begin observation. TESS' orbit around the Earth is 13.7 days, and it has 26 segments [TESS Team, 2014]. Once a segment has been observed, it is 712 days before the segment is observed again. The survey is therefore most effective at classifying variable stars with periods roughly half the 27.4 day observing window. In contrast, the ZTF aims to collect observations of the northern sky, on average, every four nights, with a $47°^2$ field of view (FOV) [Bellm et al., 2018]. As a result, it has difficulty with short period variables that would be better constrained with several observations of a target in a single night. The MOSES survey fits the niche between the rapid cadence observations in a short period of TESS and the lower cadence observations over a longer period of the ZTF.

The observations taken in the first iteration of the survey used CCD imaging in the Johnson-Cousins V-Band filter [Ward-Thompson, Derek and Butchart, Ian, 2016] and the Moses Holden Telescope (MHT). Observations were taken of a ~160x160 arcminute field, centred at Right Ascension (RA): 2h18m7s and Declination (Dec): 63°30'44". The initial goal of this project was to extend the survey by collecting more data, as well as introducing improvements to the data reduction. As this was not possible, the goal shifted to enhancement only. Improvements were made in the data reduction pipeline that allowed better photometric accuracy to be achieved. Further enhancements included an improvement to the treatment of the World Coordinate System (WCS), and the use of Gaia's EDR3 (early data release) to aid in the classification of variability.
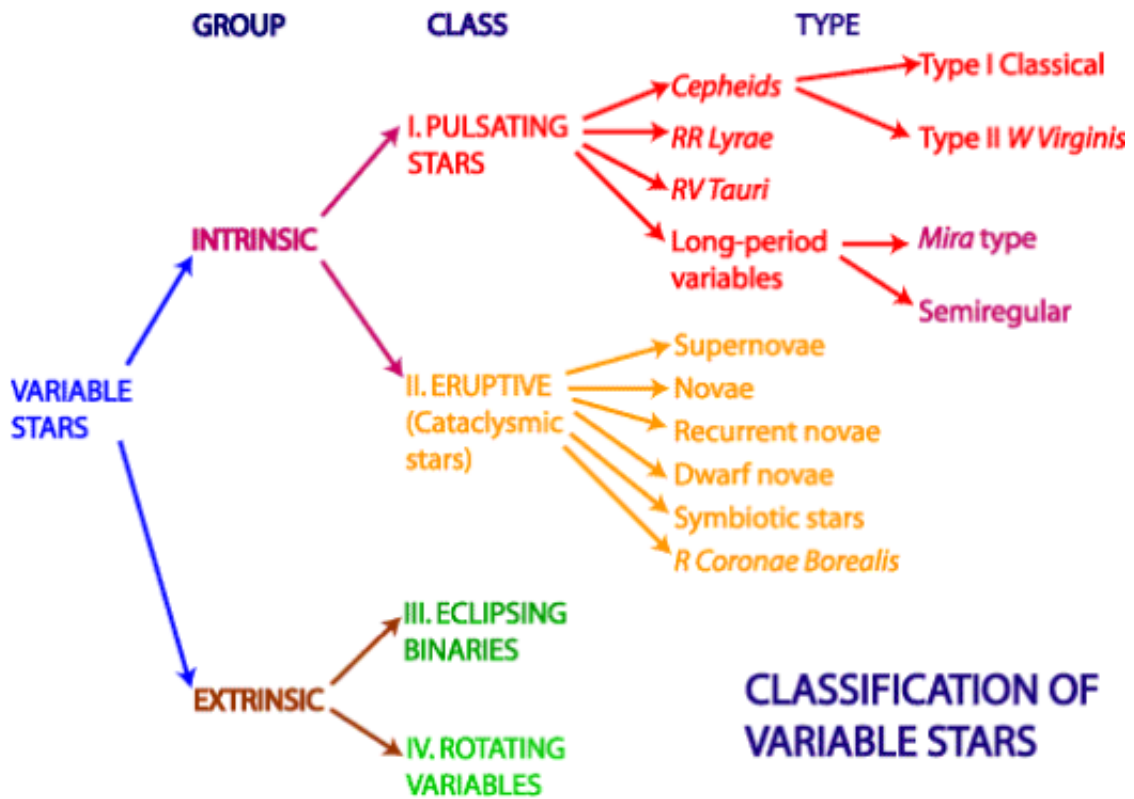
Figure 1: Variability Tree separated using the cause of variability in the system. [Australia Telescope National Facility, 2018]
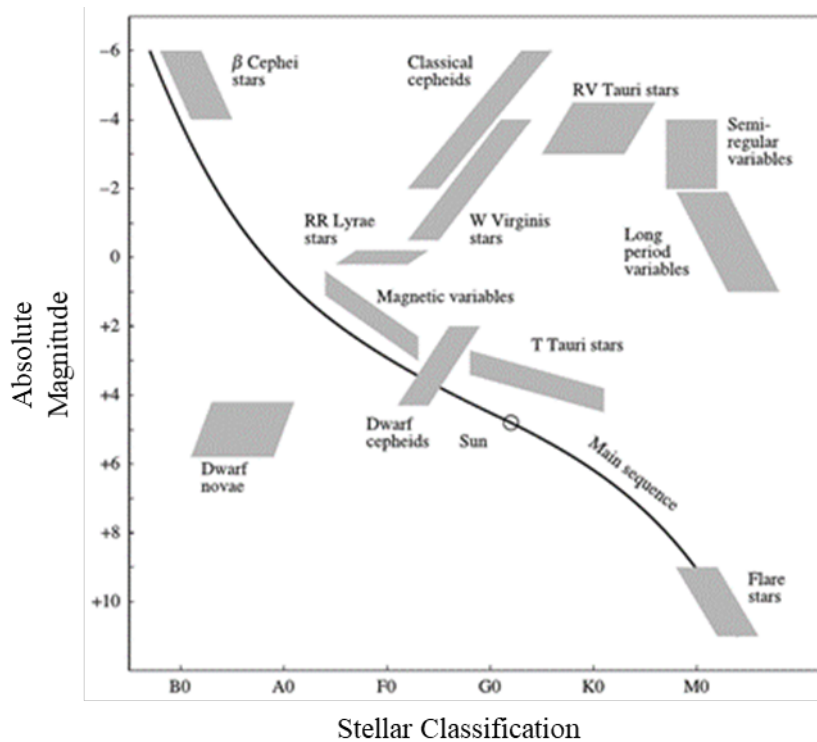
Figure 2: The position of classifications of variable systems on the HR Diagram [Karttunen et al., 2016]

2 Types of Variability

The study of variable stars provides highly useful information on the intrinsic properties of the stars themselves, as well as information that is more generally useful, such as distances. Eclipsing Binary systems show interaction between the bodies in the system, allowing masses to be calculated based on dynamics, rather than just photometrically. Cepheid and RR-Lyrae stars are useful as distance indicators in galaxies, and Mira stars are used to study stellar evolution. It is important to understand what type of variability each star displays. Figure 1, which shows the simple classification tree used as a basis in this project, displays the different types of variability. Each one can have fundamentally different causes, and different practical uses, such as providing estimates of distance or mass. Each classification of variable star has unique properties that constrain it to one of these categories. These properties include features in their light curves, such as the period, shape, or the magnitude of the change in luminosity. The position of the system on a HR-Diagram can be used to further reinforce the classification, as different classifications of variable stars lie in different regions of the HR-Diagram, as demonstrated in Figure 2. The first step for classification is to determine whether the system is Intrinsically Variable or Extrinsically Variable. It is very unlikely the survey will identify supernova, and with one observing season, long period variables will also be difficult to classify reliably as the variations could be a one time event, such as in an eruptive variable. Both Intrinsic and Extrinsic variables described below will be observed by the survey. [Percy, 2007a] provides a more in depth summary of the various classes of variable stars discussed in the following sections.

2.1 Intrinsic Variability

2.1.1 Pulsating Stars

Variability in pulsating stars is caused by an oscillation between the gravitational force pulling inwards, and the gas pressure pushing outwards being the dominant force of the star. When gravitational forces dominate, the star's outer layers collapse inwards until a point wherein pressure rises, and begins to dominate, causing the star to expand again until it reaches hydrostatic equilibrium and repeats the process.

The variation in luminosity is caused by the changing opacity during this oscillation. When the gravitational force is dominant, and the star's radius shrinks, the star is denser - there is less space between the atoms in the outer layers. Light emitted from the star's core is likely to be absorbed by these atoms before it can reach the star's surface, and be emitted. This is what causes the opacity ($\varkappa$) to increase, and the luminosity to decrease. When the atoms absorb the photons, their temperature increases. The increase in temperature causes the outer layers of the star to expand, as the gas pressure outwards begins to overpower the gravitational force, and eventually becomes dominant. The space between the atoms becomes greater - and the likelihood of a photon passing through increases - this is a decrease in $\varkappa$ and an increase, therefore, in luminosity. Figure 3 shows the positions of several pulsating variable star classifications on a HR Diagram that were observed in the Gaia Early Data Release 3 (Gaia EDR3) survey [Gaia Collaboration, 2021].
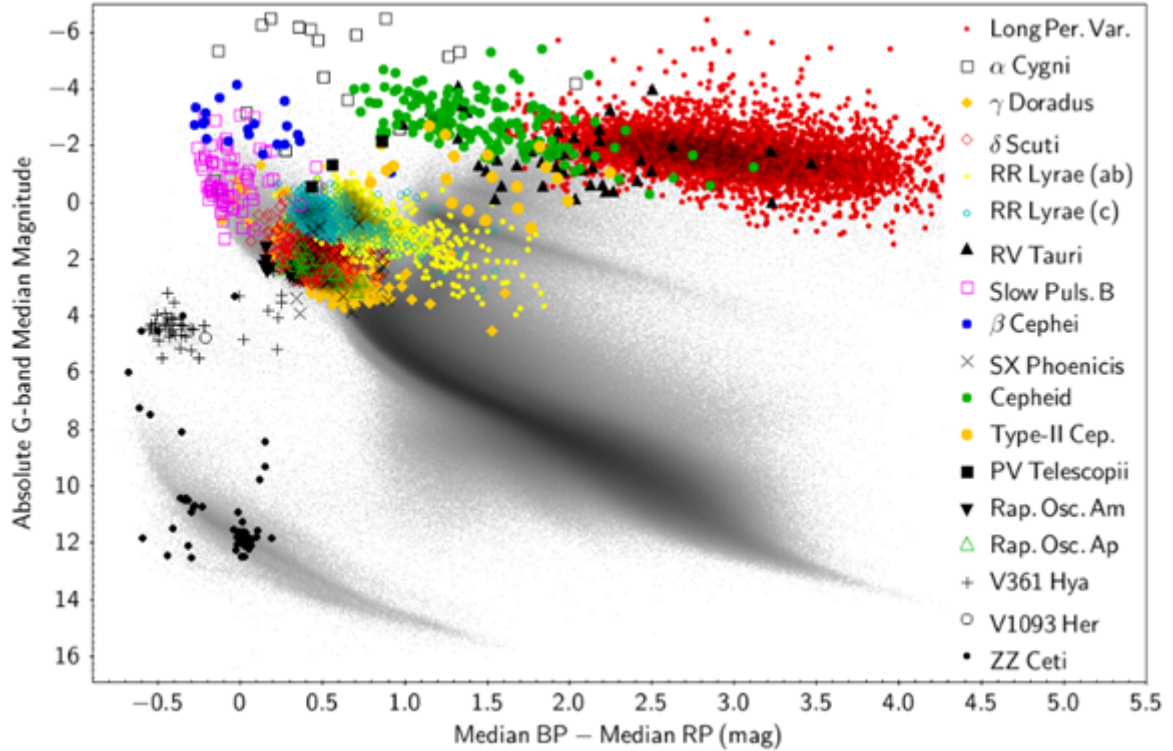
Figure 3: The position of various types of pulasting variable systems on a colour-absolute magnitude diagram (CaMD) as observed for the Gaia EDR3 Survey. It is worth noting that the blue, β -*Cephei* stars are not *Cepheid Variables* [Gaia Collaboration, 2021]

A) Cepheid Variables.
Cepheids are pulsators found on the region of the HR-Diagram known as the instability strip. Figure 3 shows their exact position, indicating that they are expected to be yellow supergiants [Anderson et al., 2017]. They are further classified into Type I 'Classical' Cepheids or Type II 'W Virginis' Cepheids - also known as δ-Cepheids. The first indication that there were two types of Cepheid is often credited to [Joy, 1937], who observed emission lines in the spectrum of W Virginis where other Cepheids had none.

Classical Cepheids are high metallicity, Population I stars with masses of 3-10M$_\odot$ [Anderson et al., 2017]. They have periods in the region of *days*, averaging around ten days. Henrietta Leavitt, noted for her work on Cepheids in the early 1900s, discovered that Classical Cepheids showed a relationship between the period of pulsation and their absolute magnitude [Leavitt and Pickering, 1912]. This relationship has allowed Cepheids to be used as standard candles by comparing the apparent magnitude with the absolute magnitude determined by the relationship.

δ-Cepheids are lower metallicity, Population II stars, with masses of 0.52-0.59M$_\odot$ [Bono et al., 1997]. Their periods are in the region of *months*. These Cepheids can be classified further into BL Herculis stars, W Virginis stars, and RV Tauri stars, based on their stage of stellar evolution, though this is more detail than the MOSES Survey will go into. δ-Cepheids have also been used as standard candles due to the aforementioned relationship. They are used to determine distances to galaxies with ongoing star formation. A consequence of Classical Cepheid's high mass is a relatively short lifetime, meaning none of them survive long enough to be present in older, non-starforming galaxies [Majaess et al., 2009].

Figure 4 [Tanvir et al., 2005] shows light curves for two different Cepheids in the Large Magellanic Cloud (LMC), the first of which has a period of 13.5 days, the second has a period of 31.1 days. The figures show the expected shape of a Cepheid light curve, a steep incline as the luminosity increases, followed by a shallower decline as the luminosity decreases at a slower rate. The shape of a star's light curve will be one of the key properties used to classify variable systems in the survey.
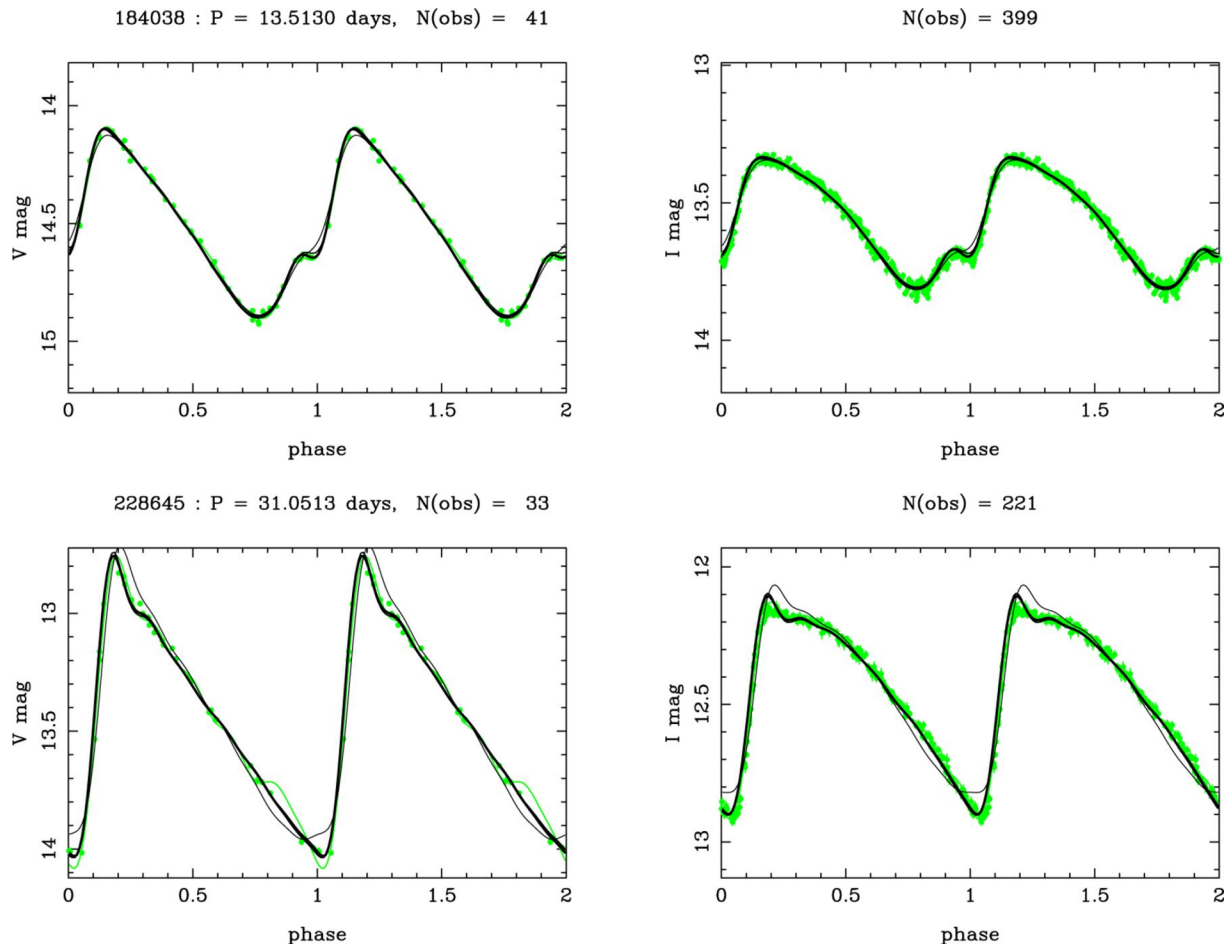
Figure 4: Observed light curves of two Cepheids in the LMC, with magnitudes given in the V-band and I-band for both curves. The Fourier fit curves are shown in grey, the black, thicker curves were constructed using principal component analysis (PCA). [Tanvir et al., 2005]

B) RR Lyrae Variables.

RR Lyrae variables lie beneath Cepheids on the instability strip, above the Main Sequence (MS) and Magnetic Variables in Figure 2. Their spectral class is in the A-F region, and they are lower in mass and luminosity than Cepheids. Like δ-Cepheids, they are Population II Stars, and have been used as distance indicators. The Cepheids overshadow RR Lyrae as distance indicators, due to the fact that RR Lyrae stars have lower luminosities, by a factor of 100, restricting the distance they can be observed to [Dambis et al., 2013]. They are, however, useful in the studies of older populations of stars. Where Cepheids have a short lifespan, and therefore exist in young, star forming galaxies, RR-Lyrae stars are lower mass, and therefore longer lived. They can exist in galaxies that are no longer forming stars. This makes them useful as measuring tools for distances to globular clusters and older galaxies in the local group. Their magnitude usually

varies by between 0.2 and 2 magnitudes, with periods in the range of hours. Their light curves are one of three shapes, depending on the type of RR Lyrae star being observed. Fundamental-mode pulsators, or RRab Stars, have periods of between 7.0 hours and 1.0 day [Soszynski and OGLE Team, 2020a]. First-overtone pulsators, or RRc stars have periods varying from between 5.0 hours and 12.0 hours, with smaller amplitudes than RRab Lyraes. Their light curves are also more sinusoidal in shape. It is common for RR Lyrae light curves to appear scattered due to the pulsation period changing during observation, primarily in stars with periods greater than 0.35 days [Soszynski and OGLE Team, 2020a]. Double-mode pulsators, or RRd Lyrae stars, have two, simultaneous pulsations. The population of RRd Lyrae in a region is dependent on the metallicity, 10% of RR Lyrae stars in metal-poor regions, such as the SMC, are subclassified as RRd stars, compared with 0.5% of RR Lyrae stars in metal rich regions, such as galactic bulges, being subclassified as RRd subclass. The two components of their simultaneous variation are a fundamental component, which displays a similar light curve shapes to RRab Stars, and a first-overtone component, which shows similar light curve shapes to RRc Stars [Soszynski and OGLE Team, 2020a]. Figure 5 shows the light curves for RRab, RRc, and RRd stars in each panel from left to right, respectively. The panel for the RRd star shows both of the behaviours in the light curve, which are then shown clearly, and separately in Figure 6.
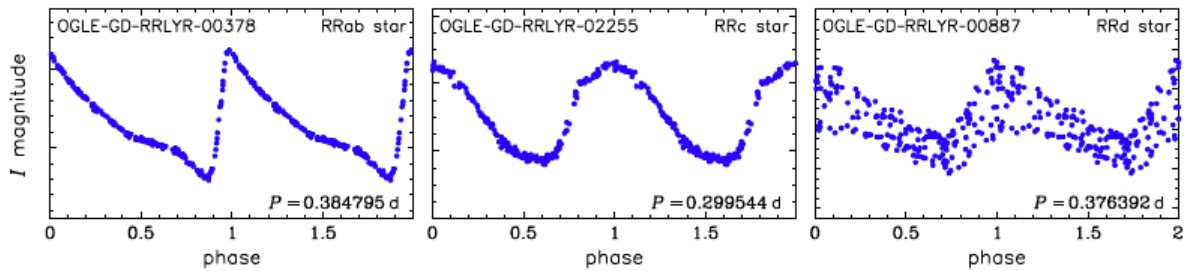
Figure 5: Light curves for an RRab Star (left) displaying a sharp increase between phase = 0.8 and phase = 1.0, and gradual decrease between phase = 1.0 and phase = 1.9. An RRc Star (centre) showing a sinusoidal shape with a smaller period and magnitude than RRab, and an RRd Star (right) displaying behaviours of both within its curve, better displayed in Figure 6. [Soszynski et al., 2019]
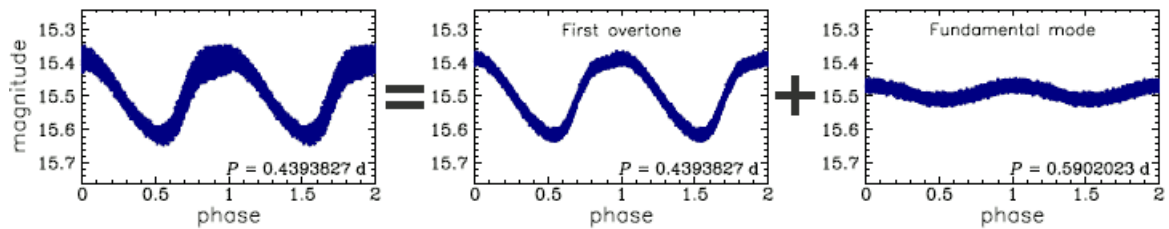
Figure 6: Light curves of an RRd Star (left). This shows the data for the first overtone component (centre), which resembles the light curve on an RRc star, and for the fundamental mode component (right), which resembles the light curve of an RRab Star. See Figure 5 for comparison. [Soszynski and OGLE Team, 2020a]

C) RV Tauri Variables.

RV Tauri Variables can be seen on Figure 2 in the supergiant branch of the HR Diagram. Typically, they have periods between 30 and 150 days [Gezer et al., 2015]. Light curves for RV Tauri stars are often confused with eclipsing binaries due to the variation in luminosity of

successive minima [Soszynski and OGLE Team, 2020b]. The deeper minimum is known as the *primary* minimum, and the shallower as the *secondary* minimum. Some RV Tauri light curves display variation in the maxima too, with the higher maxima following the deeper minima. The amplitude of the total variation can reach 4 magnitudes in the V-band [Gezer et al., 2015]. RV Tauri stars can display a second, long term variation in the mean of the luminosity. This long term variation has periods between 700 and 2500 days, roughly, and RV Tauri stars with this variation are classified as RVb Tauri stars, for which a representative light curve can be seen in Figure 7. The remainder of the population, with near constant mean luminosity, are classified as RVa stars, for which a representative light curve can be seen in Figure 8 [Kiss and Bodi, 2017]. For RVb stars, the light curve can be presented three ways, showing in Figure 7. One panel shows the star's light curve, as observed. The second light curve is folded over the star's long period - as the mean luminosity changes. This second curve is then subtracted from the first, observed curve, resulting in the equivalent curve if the star was an RVa Star, displayed in the third panel of Figure 7.
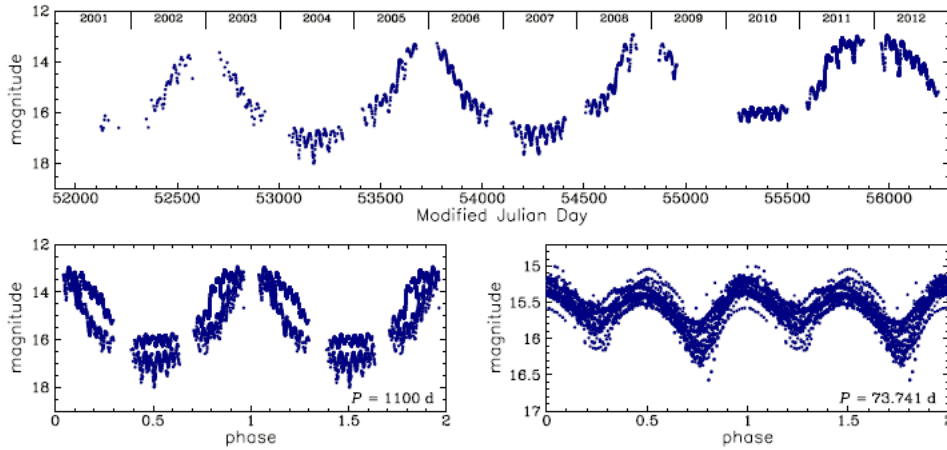
Figure 7: The light curve for the RVb Star OGLE-BLG-T2CEP-345. The upper plot shows the original light curve. The bottom left plot shows shows the star's light curve along the long period, whereas the bottom right panel shows the star's RVa Curve. [Soszynski and OGLE Team, 2020c]
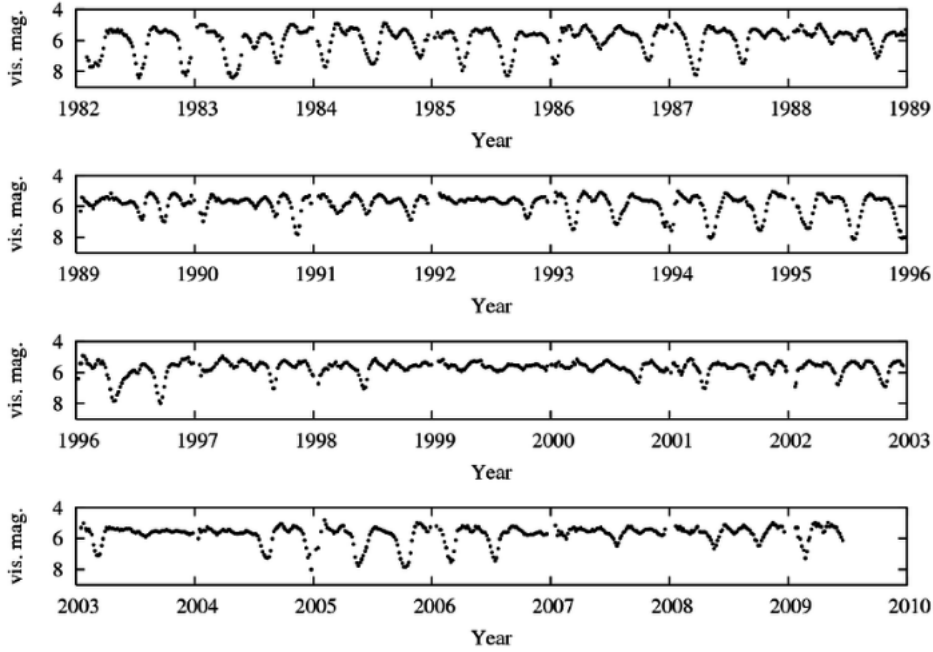
Figure 8: The light curve for the RVa Star, R Scuti, showing the alternating minima while displaying approximately constant mean magnitude [Wilson and Templeton, 2019]

D) LPV: Long Period Variables.

Long Period variables are defined by the Gaia EDR3 data as variables with periods in the G-band of longer than 60 days [Gaia Collaboration, 2021]. They lie in the giant branch, seen in Figure 2 and Figure 3, and about a fifth of LPVs are Mira type stars. The shape of a light curve of a Mira type star is sinusoidal, which allows it to be differentiated from binary star systems. Figure 3 shows the region of the HR-Diagram wherein Mira stars would be expected to lie. The asymptotic giant branch is represented by the red points in the top right. Mira type variables vary by up to 8 magnitudes in the visual wavelength [Reid and Goldston, 2002]. Approaching their minimum luminosity, though, some Miras can undergo a temperature decrease to ∼1400K, causing their light to be emitted in the infrared rather than optical, and causing a decrease in their luminosity by a factor of 1000 [Reid and Goldston, 2002]. Eclipsing Binaries could also, potentially be identified in this region of the diagram. Their light curves, therefore, will provide the differentiation between a Mira and an Eclipsing Binary. Eclipsing Binary systems have two minima in luminosity per period, that are of different magnitudes. An example of an LPV light curve can be seen in Figure 9. Semiregular variables have variations smaller than 2.5 magnitudes in the V-band. They are treated as a separate classification to Mira type stars, but there is only a small difference between the two classifications - a smaller amplitude in semiregulars, or irregular light curves [Berlioz-Arthaud, 2016] . They are multiperiodic, and so identifying them as part of the MOSES survey could prove to be significantly more difficult than other, regular classifications [Kiss et al., 1999].
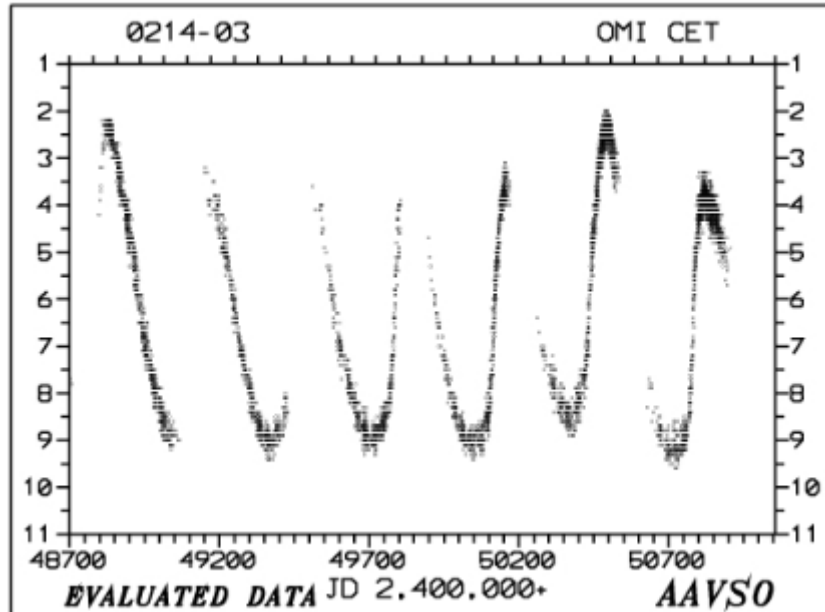
Figure 9: Light Curve for the star *Mira*, the first discovered Mira type variable, created by plotting absolute magnitude against Julian Date. It shows a variation in magnitude of roughly 7 magnitudes. [Mattei, 1996]

2.1.2 Cataclysmic Variables.

Cataclysmic Variables (or Eruptive variables) display sudden and irregular changes in magnitude. Figure 1 shows several types of eruptive variables, with novae being the most common. The MOSES Survey looks along the plane of the Milky Way (MW) where, in the galaxy as a whole, we expect 50^{+31}_{-23} Nova to occur per year [Shafter, A. W., 2017]. Supernova (SN) occur every $\sim 50 - 100$ years in the MW, and the last one (SN1604), was a type Ia SN that occured in October of 1604 [Vink, 2017]. If a star in the field of view went SN, it would definitely be seen, but the odds of seeing an SN increase greatly when observing extragalactically as it is possible to observe many galaxies, all of which contain billions of stars, simultaneously. Because the field of view is along the plane of the MW, we cannot observe stars extragalactically. Nova, therefore, are far more likely to be observed in the MOSES Survey than Supernova.

Cataclysmic variables include all classifications of Supernova as well as Classical novae, recurrent novae, and dwarf novae. All novae and supernovae, with the exception of Type II supernovae, occur in binary systems consisting of a White Dwarf (WD) and a Main Sequence (MS), or evolved star. The MS (or evolved star) fills its Roche Lobe, an example of which can be seen in Figure 13, and loses matter onto an accretion disc surrounding the WD. This causes an increase in temperature and pressure on the surface of the WD to increase until it is sufficient to cause the hydrogen layers to fuse into helium. As pressure continues to increase, eventually the helium will be converted into carbon, and so on. This becomes a runaway fusion reaction. The energy released by the reaction ejects the unburnt hydrogen from the surface of the WD, which we observe as a classical nova. Classical novae can vary by between 8 and 20 magnitudes, with brighter novae having shorter durations than their dimmer counterparts [Hameury and Lasota, 2005]. Recurrent novae undergo the same process, but are noted to have had at least two ejections within the last 100 years [Swinburne University of Technology, 2021b]. Dwarf novae occur due to a release of gravitational energy as the matter from the MS star moves through

the accretion disc to the surface of the WD. Dwarf novae have lesser magnitude variations - in the region of $2 - 6$ magnitudes [Kantharia, Nimisha G., 2017], and periods of days. This is called the Disk Instability model, and the outburst only ejects enough mass to allow the disk to become stable again [Hameury, 2020]. Dwarf novae are eventually expected to build up enough material on the WD surface to cause the runaway reaction that results in a classical nova.

Supernovae are further classified into types Ia, Ib, Ic, and II. The classifications are determined by their spectra, wherein anything with hydrogen lines is classified as a type II supernovae, and those without are a type I. Type Ia displays evidence of the absorption of Si in their spectral lines [Swinburne University of Technology, 2021d]. Neither type Ib or Ic display evidence of Si absorption, but type Ib show He emission, whereas type Ic do not [Swinburne University of Technology, 2021d]. Light curves for type Ia supernovae are also not as broad as those of type Ib or Ic [Woosley and Eastman, 1997]. The light curve for a type Ib supernova can be seen in Figure 10 in the B, V, R, I, and W bands. The light curve for a type Ia supernova can be seen in Figure 11 in the B magnitude. The light curve for the type Ia is clearly narrower than the B-band light curve for the type Ib, with the magnitude decreasing rapidly for roughly 15 days following the peak in the type Ia light curve. Type Ia supernovae occur when a white dwarf is a component in a binary star system alongside a giant star, the giant star accretes gas onto the white dwarf. A similar runaway fusion reaction to the one in classical novae occurs, hydrogen into helium into carbon and so on. The fusion reaction in a Type Ia supernova goes futher up the 'nucleosynthesis tree' and fuses heavier elements than in a classical novae. It does this as the star's core reaches far higher temperatures than the White Dwarf's surface. The outwards energy produced by the runaway reaction results in the outwards gas pressure overcoming the inwards force of gravity. The primary difference between a Type Ia supernova is where this runaway fusion reaction occurs. In classical nova, it occurs on the surface layers - the mass is ejected and the star remains. In Type Ia supernova, the reaction occurs in the white dwarf's core [Swinburne University of Technology, 2021a]. The absence of hydrogen lines within the Type Ia is due to all of the star's hydrogen being burned up into helium as part of the reaction.

Type Ib, Ic, and II supernova are fundamentally different in their formation. Over a massive star's lifetime, it burns hydrogen into helium, into carbon, and so on until the core is comprised of iron (Fe). It is then unable to fuse iron into heavier elements, as it would take more energy to fuse than it would output. As a result, the star cannot produce enough outwards gas pressure to counteract the inwards gravitational force, which becomes dominant. The outer layers of the star collapse inwards under the force of gravity, and the core compresses into a neutron star - which is in itself, uncompressable. The outer layers of the star impact the neutron star, bouncing off in an explosion we classify as a supernova.
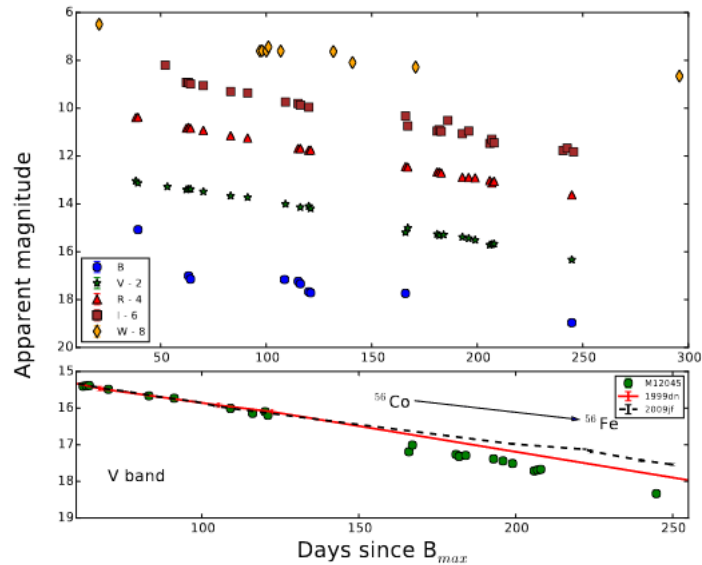
Figure 10: B,V,R,I, and W light curve plotted for the Type Ib supernova, M12045. Arbitrary offsets have been applied in each band. The bottom panel shows the decrease in apparent magnitude in the V-band compared to two other supernova, 1999dn and 2009jf. [Singh et al., 2019].
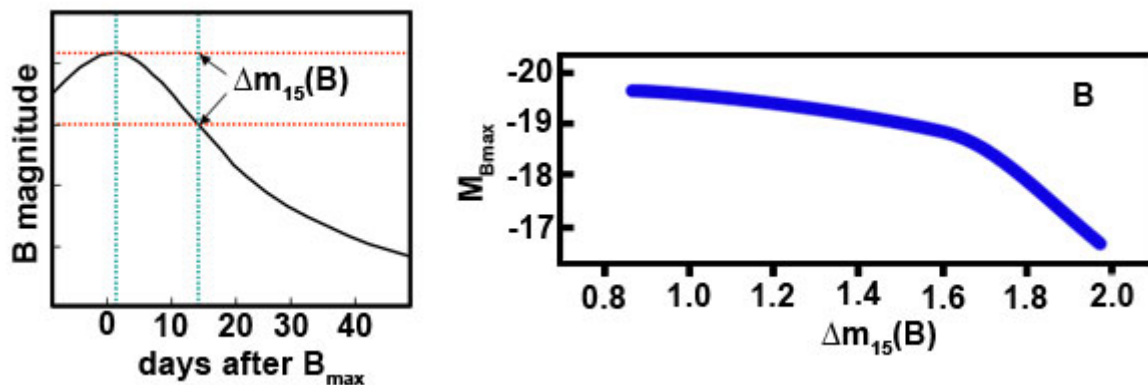
Figure 11: B-Band light curve for a Type Ia supernova. The left panel shows the B-magnitude plotted against time. The right panel shows the luminosity-decline rate relation in the 15 days after peak luminosity. Brighter supernovae are expected to decline slowly, whereas fainter supernovae decline more rapidly [Swinburne University of Technology, 2021e].

2.2 Extrinsic Variability

2.2.1 Eclipsing Binaries

Eclipsing Binary systems are systems composed of two stars orbiting around a central point - the centre of mass of the system. When one of the stars passes between the observer and the other star, it eclipses its companion, and causes the system to have a fainter apparent magnitude to the observer. Due to this, eclipsing binaries are only discovered using the transit photometry method. The variation in the system's magnitude is dependent on the size of the eclipsing star relative to the star being eclipsed, as well as the luminosity of both stars, and their separation. The light curves, shaped typically as the curves in Figure 12, have two, usually different depth minima, corresponding to the two eclipses in a period. The smaller minimum occurs when the

smaller body passes in front of the larger body, blocking out some of the light emitted by the larger body. When the smaller body passes behind the larger body, it is blocked out entirely, and the deeper minimum occurs. Temperature also effects the size of the minimum, a hot White Dwarf passing in front of a Red Main Sequence star will result in a deeper minimum than when the Main Sequence star eclipses the White Dwarf. Eclipsing Binaries are further categorised into Algol Types (EA-type), Beta Lyrae Types (EB-type), and W Ursae Majoris Types (EW-type).

EA-type systems are semi-detached systems, wherein the larger of the two stars fills its Roche Lobe, this star may lie above the Main Sequence on a HR-Diagram. The second, smaller body does not fill its Roche Lobe, and so material from the larger body is accreted onto the smaller body in the system as seen in Figure 13.

EB-type star systems are also semi-detached. The stars in these systems are not spherical, their shape is deemed to be ellipsoidal due to gravitational distortion. This distortion arrises from the closeness of the star within the system. The light curve shape in the middle panel of Figure 12 shows that there is no period of constant light - there is always a part of one of the two stars being eclipsed by the other. Despite this, the primary and secondary minima are still clearly distinguished from the rest of the curve.

EW-type star systems have two stars of similar spectral type orbiting each other, and very short periods. The period of the first W UMa discovered held a short period of only four hours [Muller and Kempf, 1903]. These systems are referred to as *overcontact systems* at times due to the proximity of the stars, which are very close together - or touching. The bottom panel of Figure 12 shows that despite it being obvious where there is a full eclipse, the EW shows similar behaviour to the EB in that the light curve does not have a flat region - the magnitude is always varying.
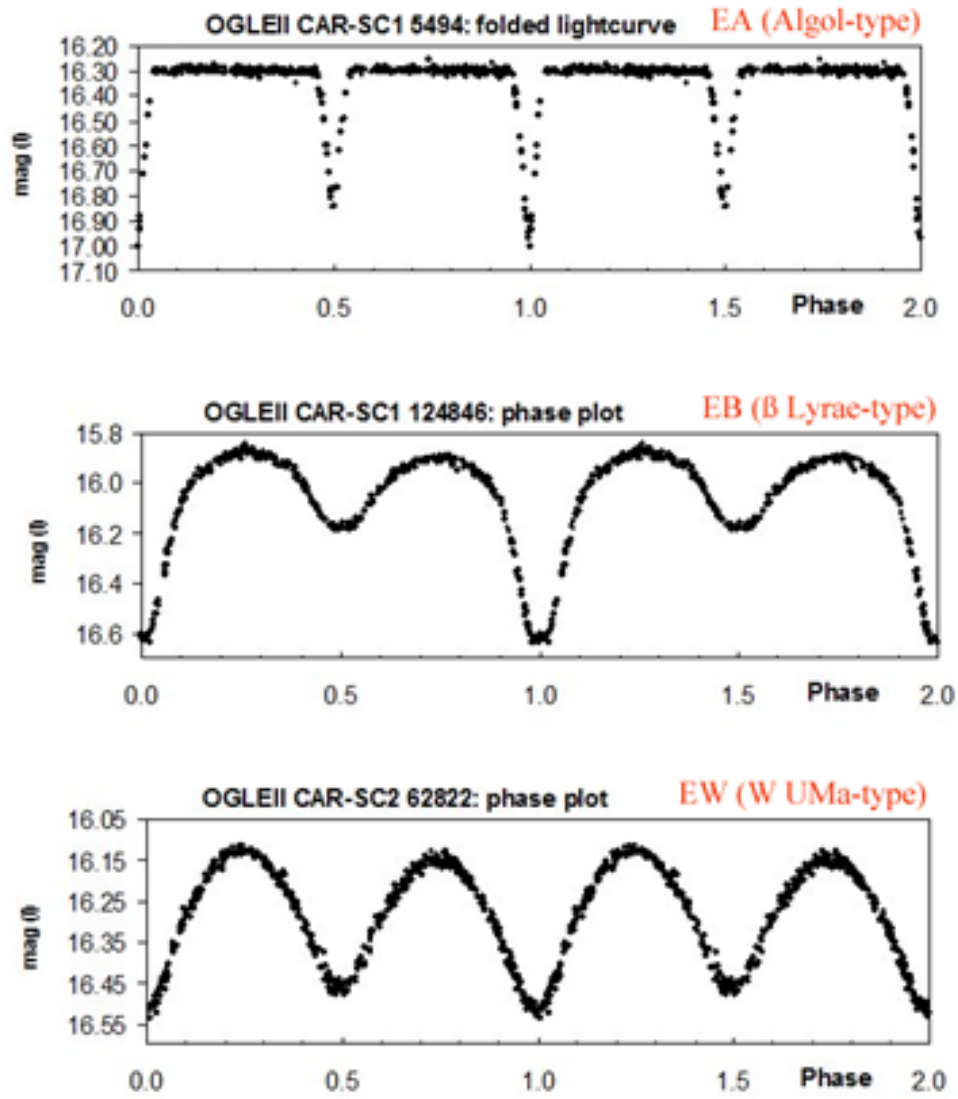
Figure 12: Light Curves for types of Eclipsing Binary Star Systems. The top panel showing the folded light curve for an EA-type. The middle panel shows the phase plot for an EB type. The bottom panel showes the phase plot for an EW type. Note the repeating, different sized decreases in brightness for each type. [Hummerich et al., 2013].
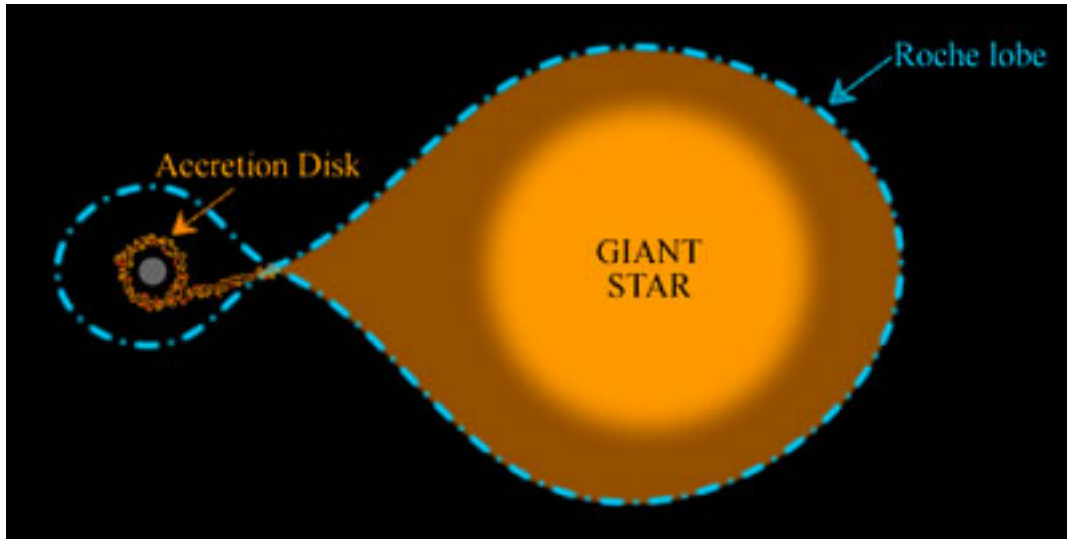
Figure 13: Simple figure showing a binary, EA-type system, in which the giant star has filled its Roche Lobe and started to lose material onto the smaller body via accretion disk. [Swinburne University of Technology, 2021c].

2.2.2 Rotating Variables

Rotating variable stars display very small variations, usually with very short periods in the range of hours [Good, 2003]. The variation in these stars is caused by the fact that stars are not uniform in flux across the entirety of the surface, and so as the star rotates, it appears to get dimmer or brighter. Sunspots, for example, cause rotating variability. In spots on the stellar photosphere where a star's magnetic field is concentrated, the increased strength in the field can cause an increase in opacity, and a drop in temperature at the surface beneath it. These spots therefore do not contribute as much to the overall luminosity of the star until the magnetic field normalises. From great distances, this makes the star look as though the flux has dropped, producing variability [Percy, 2007b]. Ellipsoidal variable systems - which are, in essence, binary star systems with elliptical shaped stars - are sometimes mistaken for rotating variables - they key being to look at the shape of the star, if it is distorted (i.e. not perfectly spherical) due to gravity, it is likely this is the effect of gravity due to an orbiting body.

2.2.3 Transiting Exoplanets

Exoplanets orbiting a star cause extrinsic variability of their host star, and their light curves present themselves as similar in shape to EA-type star systems - the larger body is the star and the smaller is its orbiting planet. The decrease in magnitude of the star is significantly smaller in value for an exoplanet than in a binary star system due to the difference in size of a star and a planet, as well as the fact that planets are not intrinsically luminous in visible light wavelengths - they only reflect light from their parent star. In the case of the top panel of Figure 12 - which shows an Algol type eclipsing binary system, the deepest minimum has a variation from 16.30 magnitudes to 17.00 magnitudes, a variation of 0.70 magnitudes. Comparatively, Figure 14 shows the folded light curves of all seven known planets in the TRAPPIST-1 system. Even the greatest decrease, in TRAPPIST-1b, shows a decrease of only 1%, or 10 millimags. TRAPPIST-1h shows even less of a decrease, at 0.5%, or 5mmag. This shows that, while the light curves of eclipsing exoplanets and stars are similar in shape, their magnitude allows us to differentiate between the two.
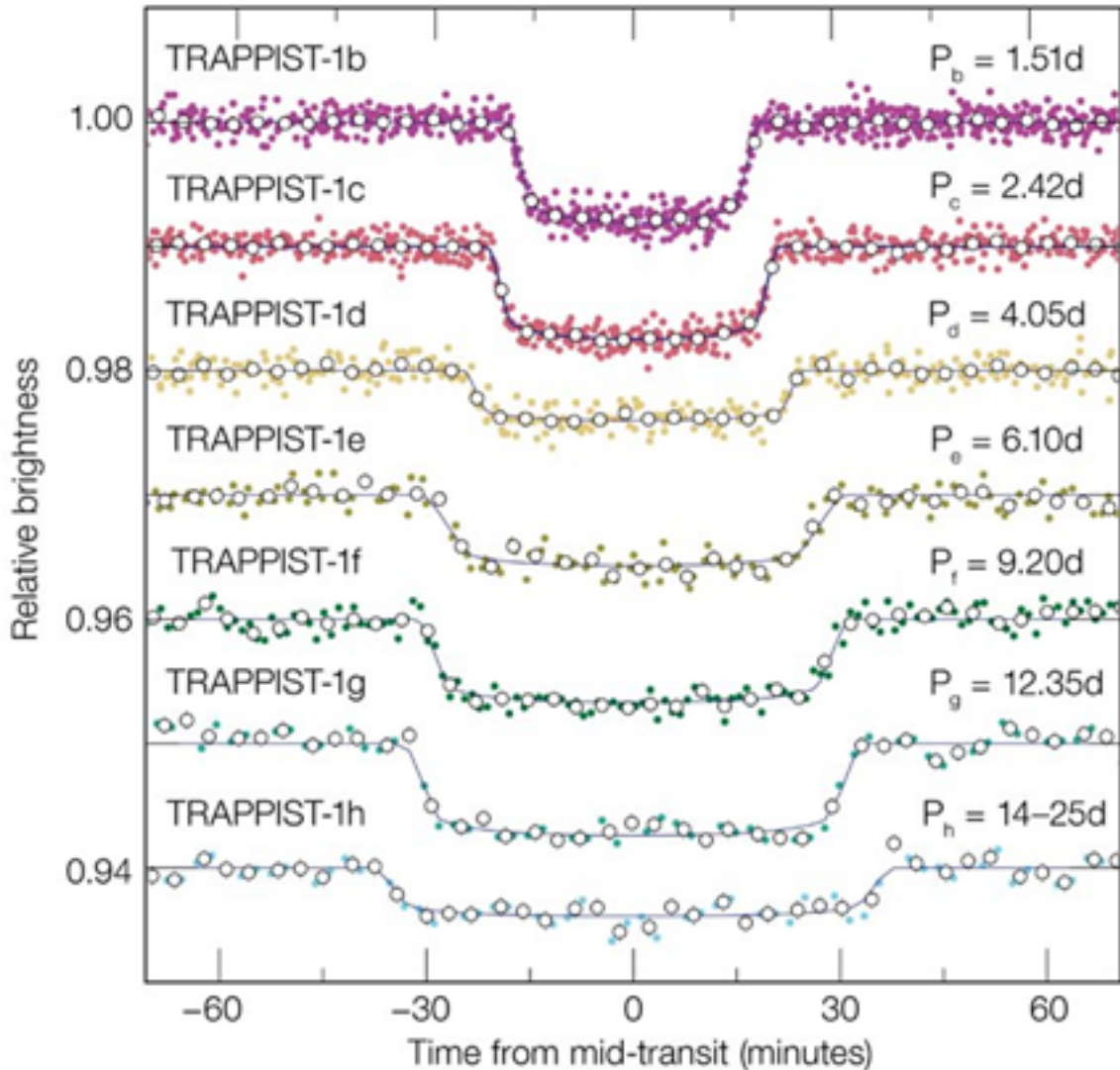
Figure 14: Light Curves of the seven known planets orbiting TRAPPIST-1. These light curves were obtained with observations from the NASA Spitzer telescope [Gillion et al. and ESO/M., 2017]

3 MHT Equipment

3.1 Hardware

Data collection was performed in the first iteration of the MOSES Survey, using the Moses Holden Telescope (MHT) seen in Figure 15. The COVID-19 Pandemic, coupled with issues surrounding a faulty dome shutter mechanism, meant that we were unable to obtain more data for this second iteration, and were forced to work only with the existing dataset. The MHT is located at Alston Observatory, at +53.80°N, and -2.59°W. The telescope is a Planewave CDK700 telescope, on an alt-azimuth mount. It has three mirrors, a primary mirror of 0.7m, a secondary mirror of 0.29m, and a tertiary mirror used to reflect incoming light into either a CCD or an eyepiece. Figure 16 shows a schematic diagram of the light path in the MHT. The MHT, when equipped with a 0.66x focal reducer and an Apogee Aspen CG16M camera, has a field of view (FOV) of ~40 x 40 arcminutes, and has a pixel scale of 1.18 arcseconds per pixel.

The *Apogee Aspeen CG16m camera* is a 16.8 megapixel sensor, made up of 4096x4096, 9µm pixels. In use, they are binned 2x2 to give the 1.18" pixel scale. It was cooled to a temperature of -35°C for the observations [Rambukwella-Gill, 2019] The Filters used in the MHT are the Johnsons-Cousins set of Ultraviolet (U), Blue (B), Visible (V), Red (R), and Infrared (I) filters [Ward-Thompson, Derek and Butchart, Ian, 2016]. The data used in the project was observed in the V band filter, using 60 second exposures for each image. The V-filter was chosen as its central wavelength, 545nm, falls in the highest quantum efficiency range for this CCD, maximising signal-to-noise [Rambukwella-Gill, 2019]. This can be seen on Figure 17 [ANDOR, 2019]

The images in the MOSES dataset had 60 second exposures. This length was selected as it provides a compromise between good signal-to-noise at fainter magnitudes, and allowing for regular repeat observations of the survey field. It takes ~22 minutes to complete a full 4x4 mosaic.

Figure 15: Image of the Moses Holden Telescope at Alston Observatory [University of Central Lancashire, 2017]
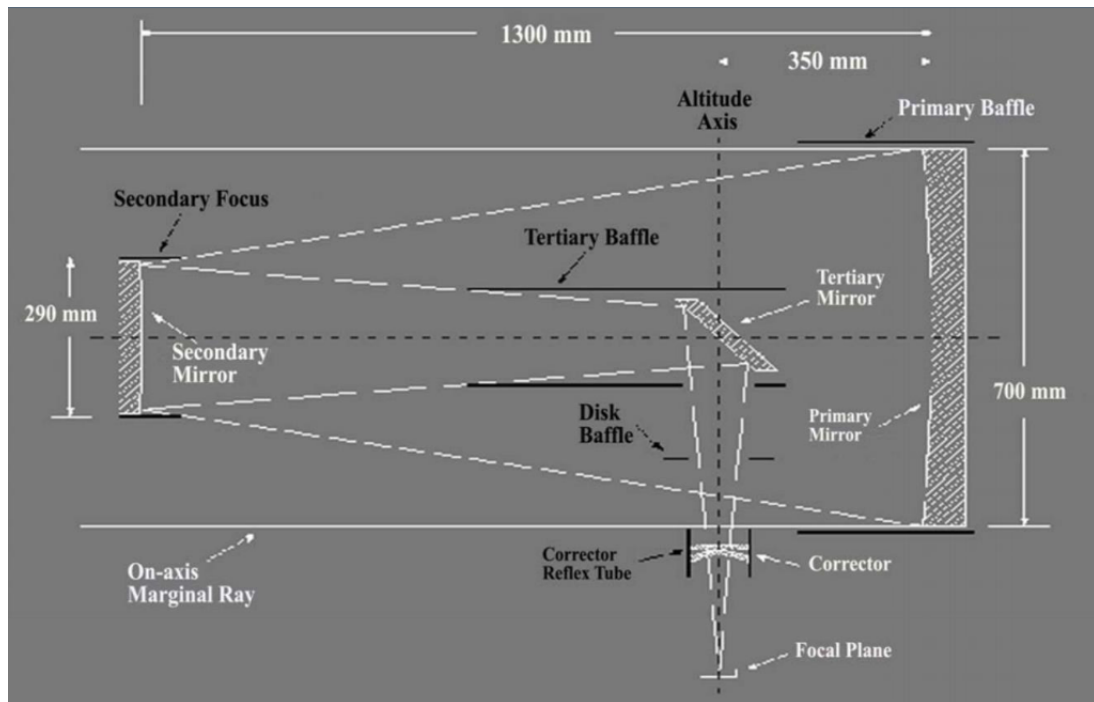
Figure 16: Drawing of the light path of the MHT. The light path is that of a Nasmyth focus, wherein light is reflected from the primary, concave mirror to the secondary, concave mirror. From the secondary mirror it is reflected onto a smaller, third, flat mirror, where it is reflected into the eyepiece or CCD. [Ward-Thompson, Derek and Butchart, Ian, 2016].

Quantum Efficiency (QE) Curve[*4]
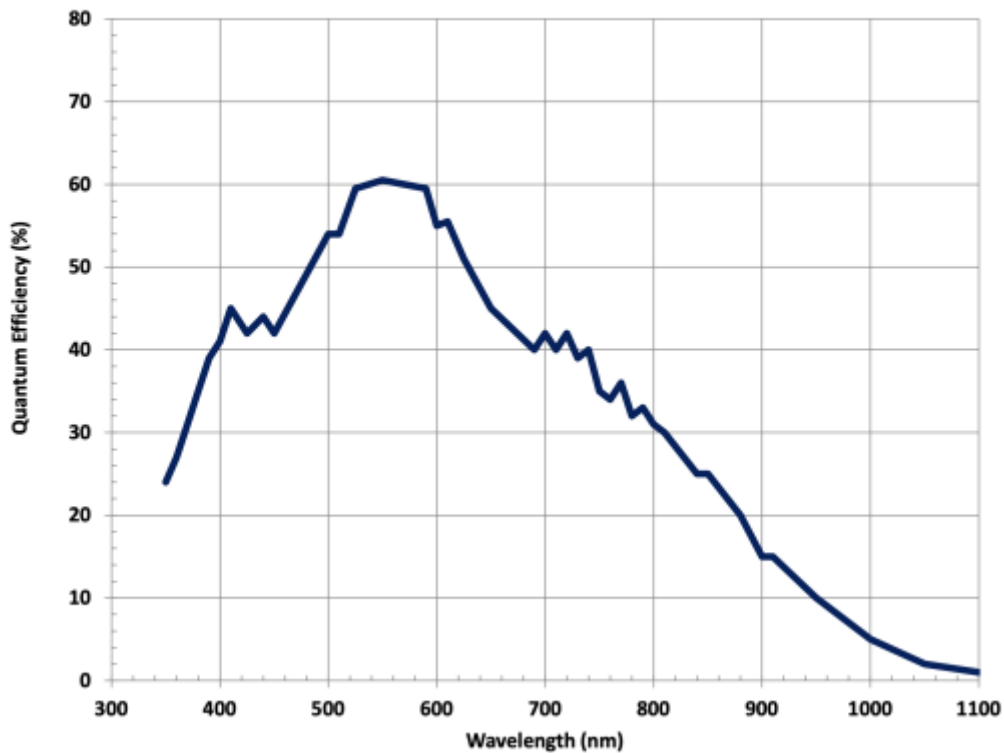
Figure 17: QE Curve for the CCD used in observations. [ANDOR, 2019].

3.2 Software

The MHT uses two software packages during observation. *The Planewave Software* is used to select the target field, and to track it through the night by moving the telescope. In doing so, it controls an IRF90 rotating focuser, that counters the rotation of the sky inherent when using an Alt-Az setup. There would be significant field rotation on even 60-second exposures, an effect that is ocassionally observed in some science images where the derotator failed. The frames are rare, and were discarded instead of being used for science. Countering the sky rotation prevents this, and in addition, allows mosaicking to be performed. The imaging pattern used during the data collection for this project was a 4x4 mosaic, seen in Figure 19. The size of the mosaic field was set by the second piece of software, *Maxim DL6*. It also controlled the filter wheel to ensure images were all taken in the V-filter, the exposure time of each image, which was set to 60-seconds, and adds a small, random offset to each image (<20"). This also ensures subsequent observations do not align perfectly, which is essential for the improved flatfielding procedure outlined in Section 4.3.

4 Results of the First MOSES Survey

4.1 Observations.

The data used in the project was obtained over the course of 25 nights of observations between October 2018 and April 2019 [Rambukwella-Gill, 2019]. Unfortunately, due to issues at the Alston Dome, and the COVID-19 Pandemic, it proved impossible to collect more data for this second iteration of the survey. More data would have been ideal, and should be a priority in any future iterations of the survey. As stated previously, the field was centred around *RA: 2h18m17s* and *Dec: 63°30'44"*. This region was selected due to its high stellar density, as the telescope points into the plane of the Milky Way, which provides more targets. Its position above Declination 60° also meant that for the observational season (October - April) it remained continuously viewable from the MHT at relatively low airmass. The region also avoids bright stars (<6 magnitudes) that risk saturation of the CCD or other issues in observation, such as reflections, glints, and persistence effects that limit the usefulness of the resulting images. Figure 18 is an image of the field, using the full moon (0.5° on the sky) for scale

The observations used a 4x4 mosaic, centred on the RA and Dec mentioned previously. 16 images were observed in sequence, and automatically named based on their position in the mosaic as shown in Figure 19. As the CCD has a 40'x40' FOV, the mosaic is 2.7° on each side. It therefore covers an area of the sky that is $7.1°^2$. Over the course of the observational season, 3998 useable images of the survey field were obtained - observing 98,580 stars at least once [Rambukwella-Gill, 2019].

Figure 18: The MOSES Observing Field (Norris, 2019).
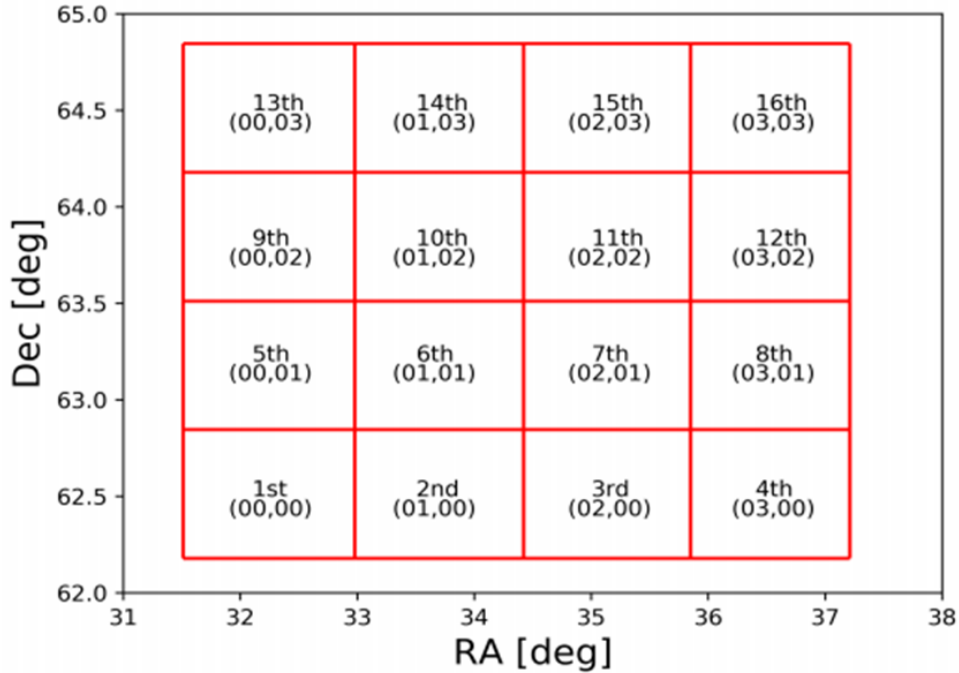
Figure 19: The layout of the Mosaic used to observe the surveying field. The imaging order, and naming convention are shown on each tile. [Rambukwella-Gill, 2019]

4.2 Results

The initial survey created a *Master Catalog* of the observations using Source Extractor [Bertin and Arnouts, 1996]. To create the catalog, a script ran through each of the images taken and stored the date and time of the image's observation in heliocentric Julian date form, and the position of the object into a Master Catalog data file. Each object within the image had its own data file created by the script to store information on it, including JD, photometry, and position. If the script found an object that was within 2 arcseconds of an object previously observed, it made the assumption that these were the same object, and appended the appropriate information to that object's data file [Rambukwella-Gill, 2019]. Using this method, the first iteration of the project detected 87,397 objects, of which 29,399 had more than 200 observations [Rambukwella-Gill, 2019]. Three cuts were then made in this data, removing objects with magnitude >17, magnitude <11, and object with <100 total observations from consideration for variability [Rambukwella-Gill, 2019]. Objects brighter than 11.5 magnitudes saturated the CCD. Objects fainter than 17 magnitudes had uncertainties that were deemed unacceptably high. Finally, with fewer than 100 observations, it is difficult to classify variability. These three cuts are displayed on Figure 20. The objects satisfied by the three data cuts had their standard deviations in magnitude plotted against their mean magnitude in Figure 21. Their magnitudes were binned into 1 V-mag width bins, and the standard deviation in the magnitude of each bin was calculated. Objects with photometry displaying standard deviations, σ, 3 times larger than the median of non-variable objects with the same magnitude, were assumed to then be variable. 719 variable objects were found using this method [Rambukwella-Gill, 2019].

A weakness of approach is in the value of standard deviation, which is affected by the presence of variable stars. We implement a different method, accounting for this, outlined in section 6.2.
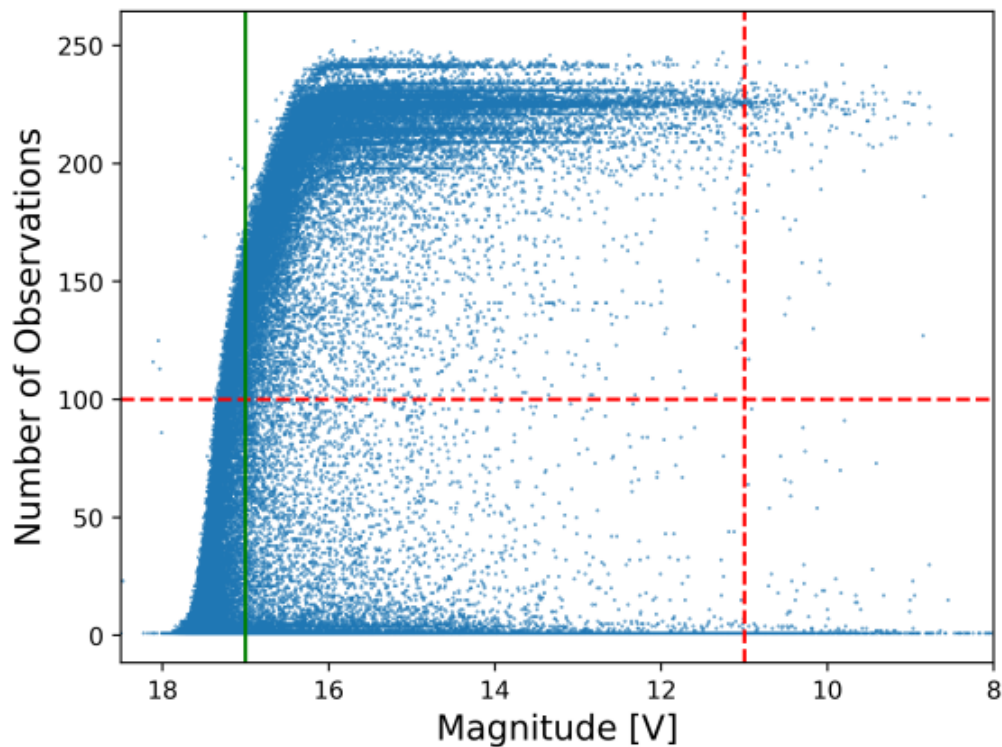
Figure 20: Plot of each object observed in the survey. Cuts in the data are displayed, cutting objects with <11 mean magnitude (vertical red line), objects with >17 magnitude (vertical green line), and objects with less than 100 observations (horizontal red line) [Rambukwella-Gill, 2019].
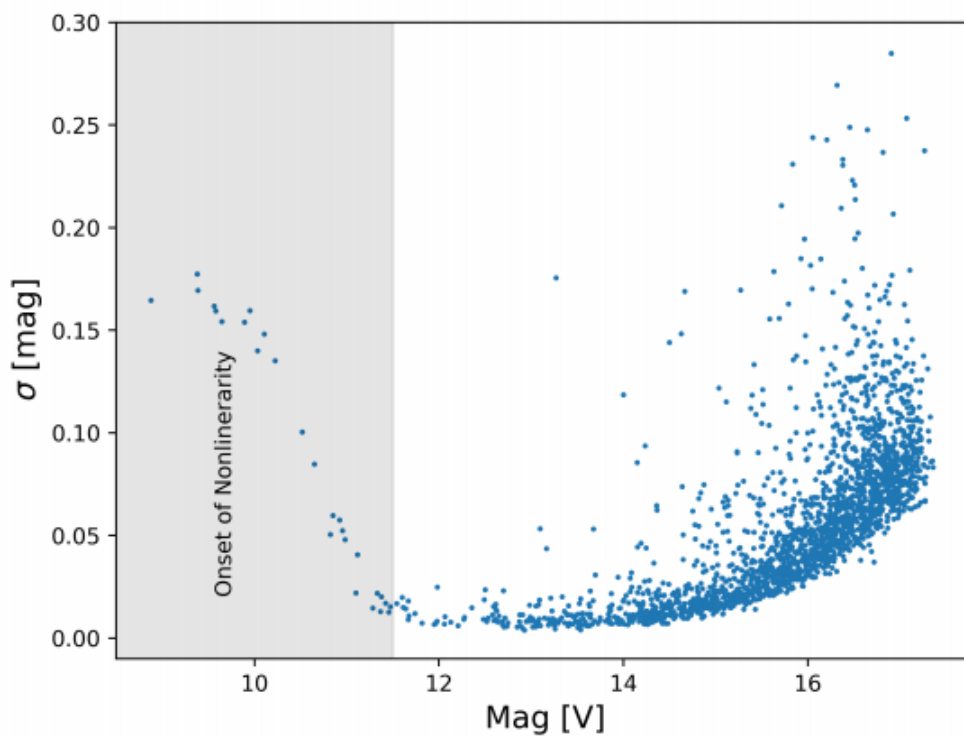
Figure 21: Standard Deviation of magnitude plotted against average magnitude for the objects observed in the MOSES Survey [Rambukwella-Gill, 2019].

5 Methodology

5.1 Improvements to data reduction procedure

Two major improvements were made to the reduction pipeline used in the first iteration of the survey. The first improvement was performed in the initial reduction stages, instead of making use of dedicated Flat Field images, this second iteration used the science images themselves to create a Flat Field Image. In the first survey, flat fielding was performed using roughly 10 twilight sky flats, taken of the sky at dusk. These Flats should be taken on the night of observation. Because this is not always possible, some of the flat field images used in the reduction pipeline had been taken up to several weeks before or after the science images. This causes issues as obstructions, such as build up of dust in the light path, will alter the flat slightly over time. The improved method produces a flat field image from the science images themselves. This means nothing has changed for the light in the flat field, relative to the science image. It has travelled through the same airmass and light path, the telescope was at the same focus for the flat field as the scientific image and the flat field was always obtained on the same night as the data.

A single mosaic used in the project has 16 pointings, and if we assume 20 observations a night, that becomes 320 separate scientific exposures. All 320 images are stacked on top of each other, and a script looks 'down' the stack at each pixel in turn. As there is a 20" random dither, even the stars from a single mosaic pointing don't fall on exactly the same pixels in each 'visit' to that particular mosaic pointing. For example, out of 320 observations, each pixel in the stack may lie on a star roughly 40 times, when this happens the script recognises the outliers due to their brightness and rejects them, as a pixel with light from a star will always be brighter than one with just light from the sky. It then takes a median value for the remaining pixels. This procedure is repeated for every X,Y pixel, producing the 2D flat field. The entire raw flatfield frame is then normalised by dividing it by the median value of the image. This technique is often employed when observing in the Infrared due to the high sky background, as it provides sufficient flux to produce high signal-to-noise flatfield images. In this case, the method works for our optical data due to the relatively high brightness of the sky at Alston when compared to a professional observatory, as well as the large number of individual frames.

Figure 22 shows the improvement, where the points plotted with the previous Flat Fielding method have higher standard deviations on average than those with the improved method. The standard deviation, in this case, displays variability in the apparent magnitude, but the points plotted are for stars confirmed to *not* be variable using the method outlined in Section 5.2, so any deviation from the mean is due to noise. The blue points on the figure show the stars that were determined to be non-variable in reanalysis, resulting in the clear edge. The red points are the same stars with the photometry from Rambukwella-Gill, but due to the differences in the reduction process, their uncertainties are signficiantly higher for a subset of stars, and therefore do not have the sharp edge. The median decrease in scatter between the red and blue points is ~0.4millimags, though the improvement is greater than 5mmag in ~13% of cases. This relatively small improvement could prove significant in the identification of transiting exoplanets, as it could be the difference between the script incorrectly identifying photometric errors as exoplanets, or dismissing variation due to exoplanets as photometric error.
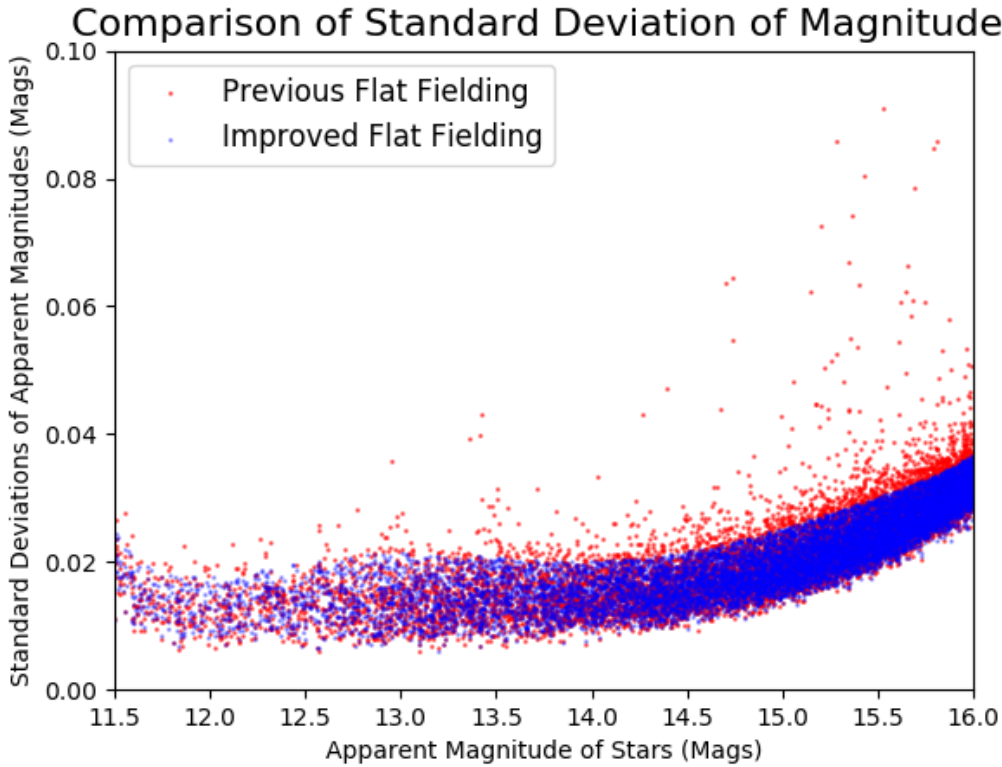
Figure 22: Standard Deviation of magnitude plotted against average magnitude for nonvariable objects observed. The Red points show the previous Flat Fielding Method, while Blue Points show the improved method.

The second improvement was made due to issues with the World Co-Ordinate System (WCS). The telescope has a curved mirror, so it produces a curved focal plane during observations. We cannot optically flatten the plane perfectly at large angles, such as those in the corners of the images. Because the CCD is flat, though, the centre of the image can be focussed on the CCD well, but the edges cannot also be perfectly in focus because it is tracing a curved focal plane onto a flat CCD. This means that the pixel scale of the image varies slightly as a function of the pixels on the chip, leading to distortions in the corners of the image.

The software that determines the WCS in MAXIM DL [MaxIm DL, 2021] assumes the WCS is linear in all directions, so the pixels are both square, and the same angular size in all positions. This assumption means the calculated position of the stars in RA and Dec become progressively less accurate moving away from the image centre. The reduction pipeline refits the WCS with a non-linear WCS (Single Imaging Polynomial, 'SIP' convention) using astrometry.net to account for distortion. However, Source Extractor (SExtractor) [Bertin and Arnouts, 1995], which measures the photometry, uses the TPV WCS Standard [Calabretta and Greisen, 2002]. Coordinates returned by SExtractor, therefore, do not account for distortion as it does not understand the Astrometry.net convention. Previously, corrections to the WCS were made by taking the X, Y pixel coordinates from SExtractor, and then calculating RA and Dec using the astrometry.net WCS and python. This approach was slow, and the correction was not suitable for mosaicking. SWarp [Bertin et al., 2002], the software used to coadd images, uses the same TPV standard as SExtractor. The previous matching method does not fix distortion in the images themselves, therefore it did not allow for mosaicking using SWarp. We implemented a python script that

converts the astronomy.net SIP convention into a TPV one that Astromatic software [Bertin and Marmo, 2021], such as SWarp and SExtractor can understand. This will allow for future projects to produce deeper coadded images, possibly of entire nights. This will allow for searches for fainter objects, including variables and slow moving solar system objects. Figure 23 shows a zoomed in version of the MOSES Field with no WCS correction, highlighting the need as there is duplicate stars where tiles overlap.

Figure 23: Zoomed in version of the MOSES observing field where two mosaic tiles overlap. The highlighted region shows more clearly the duplicated stars before the improved reduction process was applied (Norris, 2019).

5.2 Reduction & Catalog

There were 28 nights of observation in the initial iteration of the survey [Rambukwella-Gill, 2019]. The data, alongside dark field and bias field images, was organised by night and run through the reduction pipeline. Dark Images are taken with the telescope's shutter closed to obtain estimates of sources of counts in the image caused solely by the equipment, for the MOSES observations, these Dark images all had an exposure time of 60 seconds, the same as the scientific

images. As discussed in section 4.3, improvements had been made to the pipeline that negated the need for separate flat field images. The Dark image was subtracted from the science image, which was then used to create the flatfield images. The science images were then divided by the normalised flatfield. The pipeline renamed the fit files based on their Julian Dates for better organisation. There were 3998 *.fits* files that had been reduced and renamed. Originally, there were 4021 - but some were found to have images in the B filter, rather than the V filter like the rest of the observations, and others suffered derotator failures. These images were removed. A script was used that ran SExtractor on each image to detect objects, and created a *.csv* file for each object containing necessary information - the apparent magnitude, error in the apparent magnitude, time the image was taken etc. New *.csv* files were created when new objects were detected, and matches between existing objects and objects detected in the frame were determined by a matching radius of 1.0" on the sky.

A second script then cycles through these .csv files, appending the RA, Dec, name of the file, and length of the file to respective lists. The length of the csv file shows how many times an object had been observed. The script then obtained the magnitude values from the csv files, removing any occasional *'Not a Number'* (NaN) values. The errors in these magnitudes were also obtained, and underwent the same process to remove NaN values. The median values for both the magnitude, and error in the magnitude, were then appended to their respective lists. The standard deviation in the magnitudes (once their NaN values had been removed) were then appended to a final list. The script had to perform two separate instances for this loop, as some objects had length values of 1, and were causing errors in the script due to miscommunication between python and pandas. Once the necessary information was extracted from the csv files and appended, there were seven parameters listed for each object (Name, RA, Dec, Magnitude, Error in the Magnitude, Standard Deviation of the Magnitude, and Length). These lists were written into another csv file - the catalog. There were over 98,580 csv files that the script needed to cycle through to complete the catalog.

5.3   Identifying Variables

The method for finding variability implemented was an improvement upon the method in the last iteration as it takes into account the effect variables have on the expected photometric scatter a star of a given magnitude displays. For the purpose of the project, variables were defined as an object whose photometry had a standard deviation of greater than, or equal to 3σ compared to the mean observed standard deviation displayed by the stars in that magnitude bin. There are, of course, variable stars in the data set with standard deviations of less than 3σ, only more accurate photometry and more images will allow us to find them. Using the catalog of all objects, Figure 24 was created. This is the same plot as Figure 21, taken from [Rambukwella-Gill, 2019], but with the improvements to photometry. In Figure 24, all of the objects with greater than 100 observations were plotted first, shown in green. The plot should display a linear trend, but it is clear that it does not at values with magnitudes dimmer than 16, and brighter than 11.5. Cuts were made here, as anything brighter than 11.5 magnitudes can cause saturation of the CCD, and anything dimmer than 16 magnitudes cannot be reliably observed with this data set - though more data collection and a longer baseline will allow the dimmer objects to be analysed more reliably. The points that met those three criteria were plotted in blue. Next, the data were organised into bins of 0.125 magnitude width. The median magnitude of each bin, and median standard deviation of the photometry of the stars in the bin, were plotted as the red line on the Figure.

The 16th percentile (i.e. the standard deviations of the least variable 16% of stars in each bin) was then plotted in blue, and corresponds to $\sim 1\sigma$. If there was no variability whatsoever, the standard deviation of the photometry would be driven by photometric noise, so plotting the 84th percentile (16% of the points lie above this line) would give a mirror of the 16th around the median standard deviation, this was plotted as a dashed blue line on Figure 24. This shows the distribution was not symmetric, the 84th percentile was not the 16th mirrored around the median. Many more objects had anomalously high standard deviations, due to their variability. Since it was decided that objects above 3-sigma were to be considered variable, the 16th percentile line was mirrored about the red, median magnitude line. The distance between the mirrored 16th percentile line and the median line was then tripled - giving the purple line labelled *Median + 3*(Median-16th percentile)*. This line therefore represents the '3σ' standard deviation in the magnitude. The yellow line on Figure 24 shows the value of 3σ obtained before taking into account the effect of the variables. This is equivalent to the approach used by [Rambukwella-Gill, 2019], and results in fewer variables being detected. Objects between this line, and the purple line representing the improved 3σ are variable stars that the previous method would have failed to identify. A sample of ten stars from this region were selected, and checked to ensure they are true variables.

Three different groups of variable stars were highlighted on the diagram, the "least variable variables", with standard deviations between 3σ and 5σ in pink. The "most variable variables", with standard deviations greater than 7σ in black. Then, variable stars between these categories, with standard deviations between 5σ and 7σ - plotted in purple. For the analysis, and the remainder of this project, we focussed on the greater than 7σ variables, though future projects could study more in depth the 3-5σ and 5-7σ regions. Finally, the script wrote three csv files - one containing every variable star with greater than 3σ , one with every star with greater than 5σ , and one containing solely the $>7\sigma$ stars. The method found 764 objects that had standard deviations between 3σ and 5σ, 249 between 5σ and 7σ, and 482 with $>7\sigma$, for a total of 1495 objects.
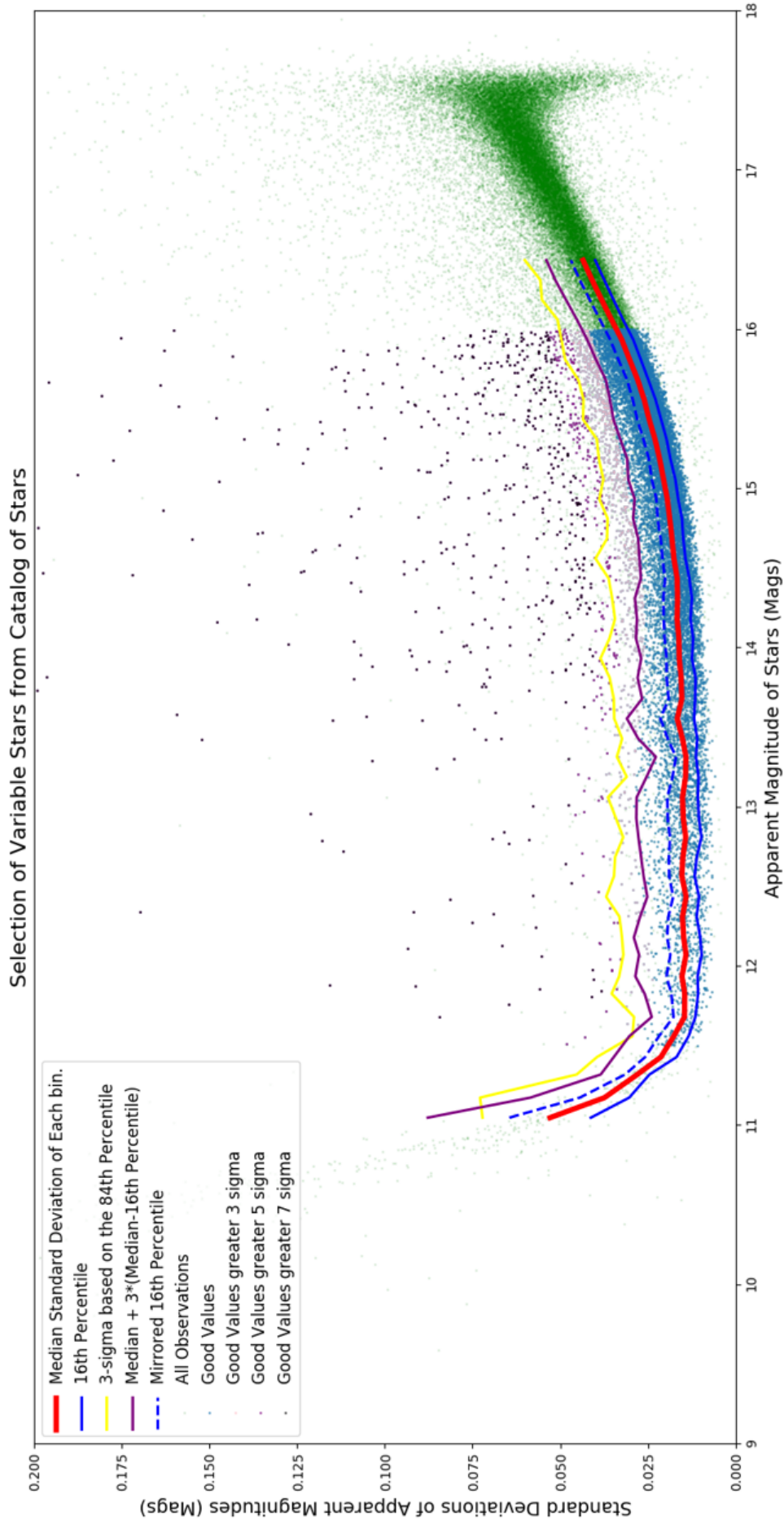
Figure 24: Standard deviation of magnitude against magnitude to obtain this plot. Objects with >3-sigma are highlighted, and have been identified as variables.

5.4   HR-Diagram

With the variable sample assembled, one way to classify the stars is based on their position on a HR-Diagram. The plot in Figure 26 shows the construction of such a diagram using a combination of the MOSES Data, and data from the Gaia EDR3 Release [Gaia Collaboration, 2021]. The Gaia data was unavailable in the first iteration of the survey, so did not form part of that analysis. The script used to create the figure first reads in the catalog file containing data on every object identified in the survey. The Gaia catalogs used keep their distances and photometry in different locations. The script tells the catalogs that any two objects with a distance of less than 1 arcsecond between them on the sky should be treated as a single object, then returns a single "Gaia Catalog" with all the necessary information. The process of matching two catalogs is then repeated for the complete Gaia Catalog, and the MOSES Catalog. A dustmap package was imported [Green, 2018] to obtain values for the extinction due to dust between the object, and the observer. The package uses the Bayestar19 3D dustmap [Green et al., 2019], which corrects for extinction as a function of RA, Dec, and distance to the object. Coefficients were applied to the extinction values to convert from the magnitude in E(g-r) to the G_{BP} and G_{RP} filters. The correction coefficients were 2.74 in the G-band apparent magnitude (G_{mag}), 3.374 in G_{BP} and 2.035 in G_{RP} [Casagrande and VandenBerg, 2018]. Figure 25 shows the Gaia HR-Diagram before the application of the extinction corrections. There is a noticeable difference on both axis, as the correction causes a decrease in the BP-RP value and a decrease in absolute magnitude. This leads to the tighter red clump and more reasonable main sequence on Figure 26.

The apparent magnitude was converted into an absolute magnitude using the rearranged form of the equation $m - M = 5log(\frac{d}{10})$. The plot is then created by plotting absolute G-magnitude against Colour (BP-RP). This process is then repeated for the catalogs that were created with the identified variable stars, and overplotted on the same figure. In Figure 26, the script was first run to plot all variable stars identified by the survey, stars with $>5\sigma$ and then $>7\sigma$ were then both overplotted to show three groups. Figure 26, Figure 2, and Figure 3 can then all be compared to aid in the classification of a variable star. Figure 27 shows the HR-Diagram with only the variables that displayed the greatest change in luminosity ($>7\sigma$). Another MRes Project this year by [Cullen, 2021] focused on identifying Eclipsing Binary stars (EBs) in the catalog created in the first iteration of the survey [Rambukwella-Gill, 2019]. The confirmed EBs are highlighted on Figure 27, and are generally included in our 7σ sample due to their high variability.

The position of the most variable stars on Figure 27, compared with Figure 3, tells us that when looking at the light curves of these stars, we would expect to see the expected light curve for Mira Stars or Eclipsing Binary systems. Figure 3 also shows that there is a chance we would see the expected light curve of a Classical Cepheid or an RV Tauri star in this region, though this seems less likely than observing a Mira Star. There is a strip of $>7\sigma$ stars along the Main Sequence. Literature informs us that neither Classical Cepheids nor Mira variables should be Main Sequence stars. We can therefore expect that the light curves for these objects will be those of Eclipsing Binary systems. These types of stars are expected because of the large magnitude variations they display, resulting in the $>7\sigma$ standard deviation.
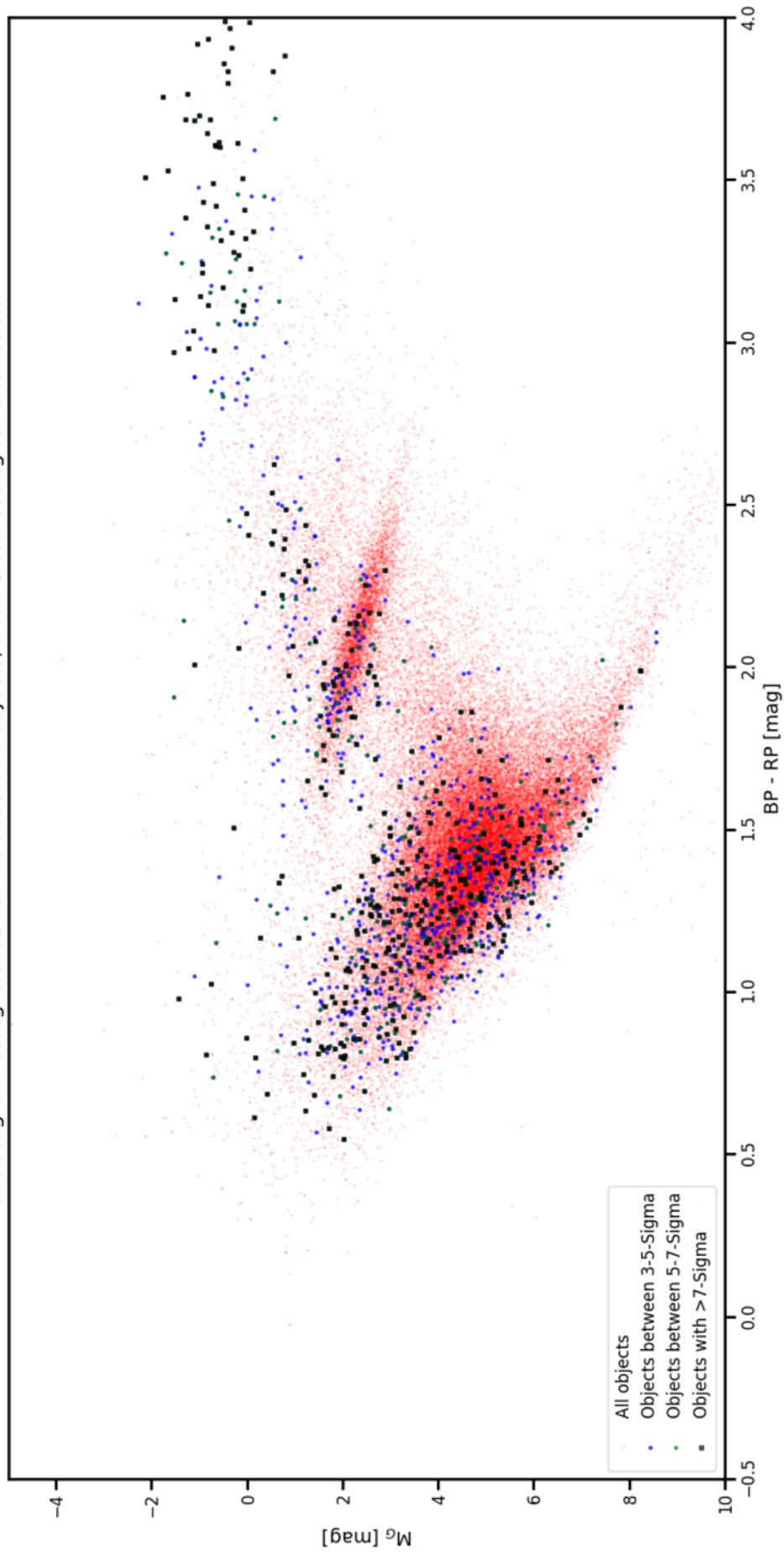
Figure 25: HR Diagram created using the positional data from the Gaia EDR3 Dataset for the objects observed in the MOSES Survey before applying corrections for extinction based on [Casagrande and VandenBerg, 2018] and [Green et al., 2019].

Figure 26: HR Diagram created using the positional data from the Gaia EDR3 Dataset for the objects observed in the MOSES Survey after applying corrections for extinction based on [Casagrande and VandenBerg, 2018] and [Green et al., 2019].
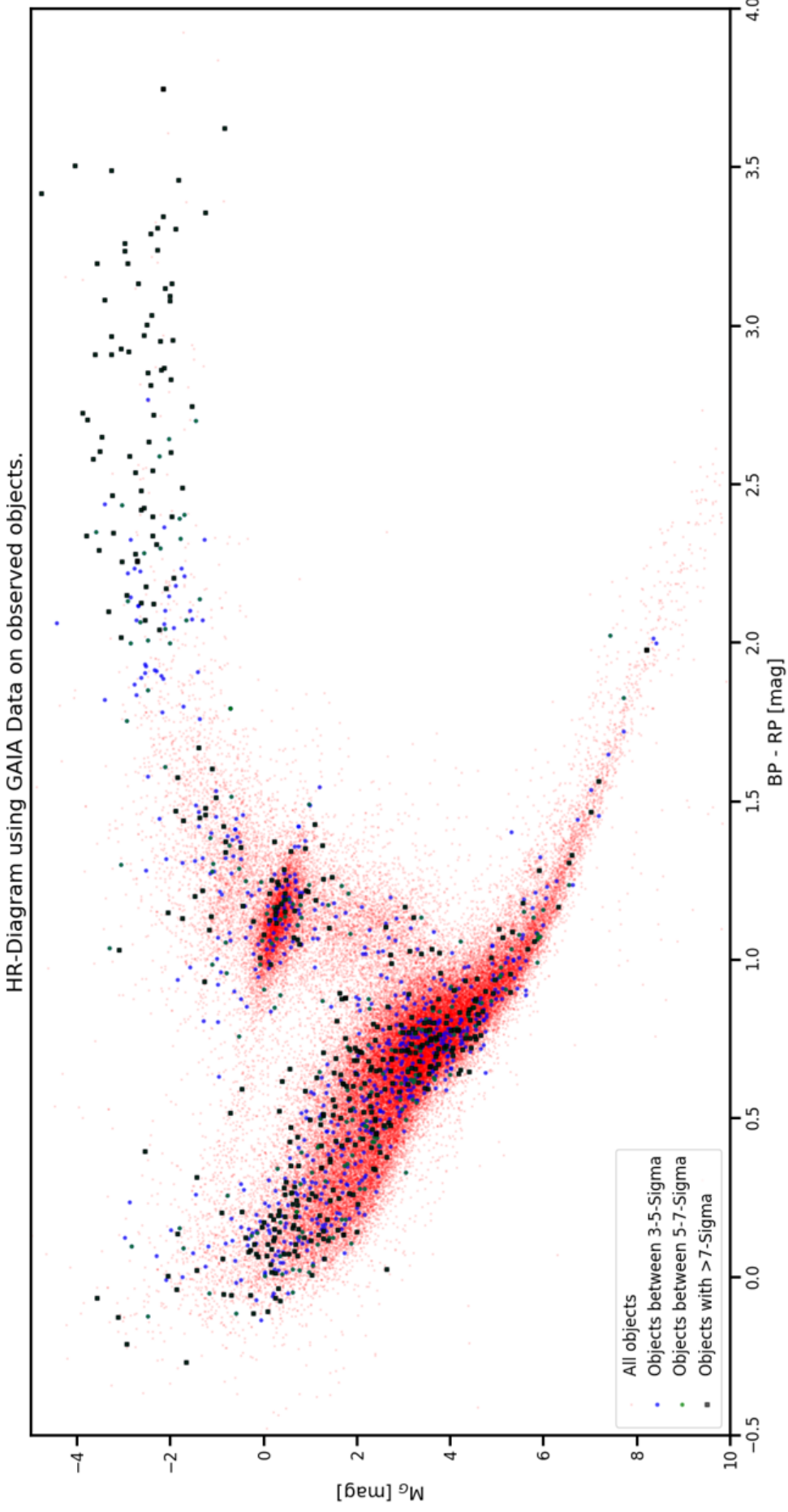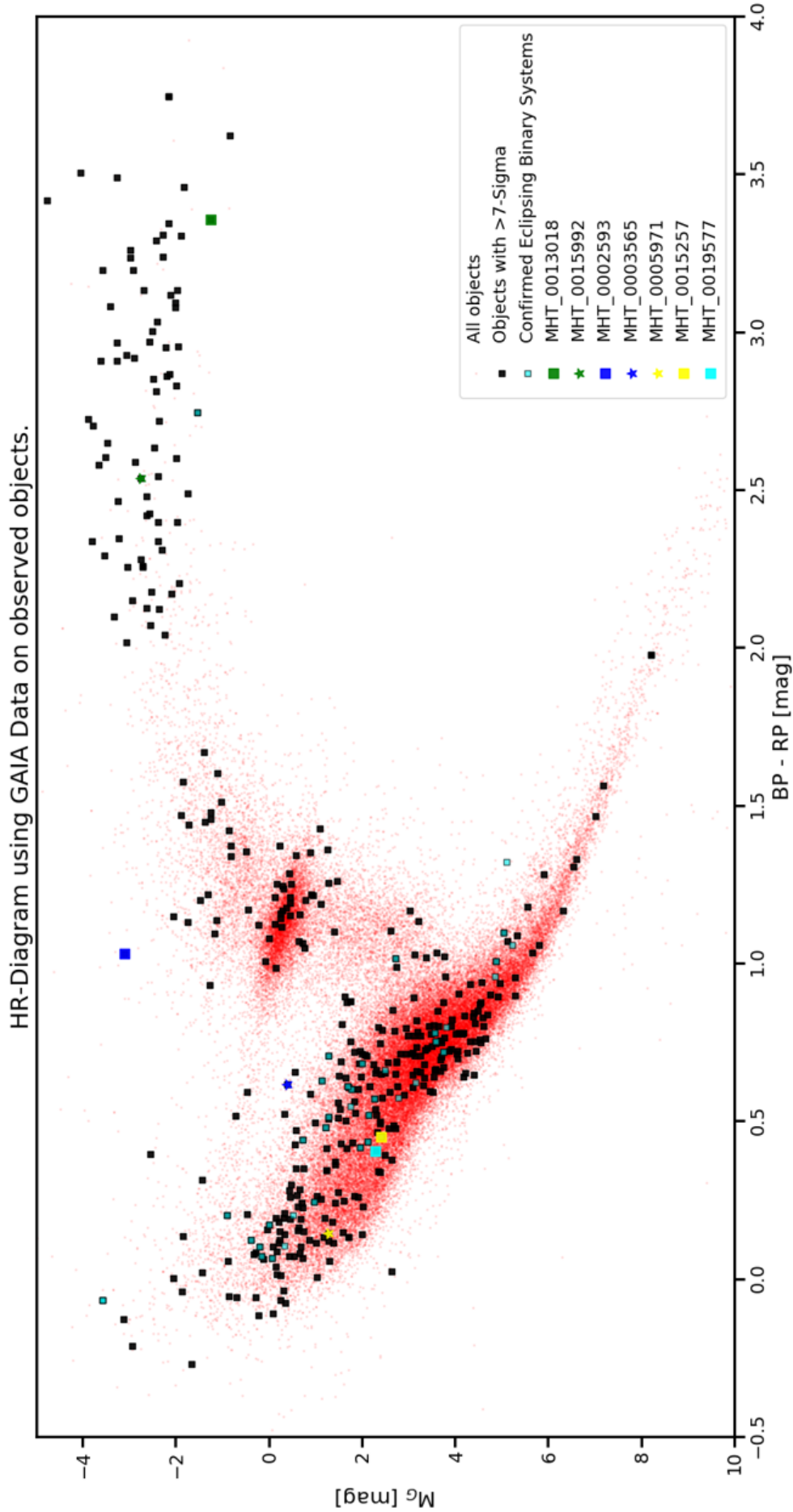
Figure 27: An annotated version of the HR-Diagram in Figure 26 showing the variables with $>7\sigma$, as well as the objects confirmed to be EBs by [Cullen, 2021], and the stars used in analysis in this section.

5.5 Light Curves

This section shows a selection of the 7σ variables, drawn from across the HR-Diagram, to demonstrate the power of adding the Gaia EDR3 data to the MOSES data. The selection was chosen to provide examples of all the potential variable classifications that would be expected in the >7σ group, according to Figure 3. Obtaining the light curves, and the periods, for each object in the selection, highlighted in Figure 27, was done using a Lomb-Scargle script [VanderPlas, Jacob T., 2018]. By analysing only the >7σ group, we limit ourselves to only the most variable stars. Based on their position on the HR-Diagram in Figure 3, and the need for large variations (>7σ) in magnitude, these stars are expected to be Mira type stars, or eclipsing binary systems, with the potential of finding Classical Cepheids and RV Tauri stars, too. The period output was checked against a pulse-density modulation (PDM) script described in the thesis of another MSc (Res) student [Cullen, 2021].

For the variables in the dataset that we classify as Cepheids, the Period-Luminosity (PL) relationship was utilised as further reinforcement for the classification. We used The PL relationship found by [Groenewegen, 2018], who cites it to be $M_V = -2.20log_{10}(\text{Period[days]})$ - 2.05

5.5.1 MHT_0002593

MHT_0002593 lies in the red giant branch of the HR-Diagram, at the top of the instability strip. It has a BP-RP value of ∼1.0 magnitude, and an absolute magnitude of ∼-3.0 magnitudes. The light curve, shown in Figure 28, shows a sawtooth shape with a variation of ∼0.51 magnitudes, between ∼13.12 magnitudes and ∼13.55 magnitudes. This shape light curve is suggestive of a classical Cepheid star, or of an RRab Lyrae star. Figure 3 reinforces either one of these classifications, with its location on the HR-Diagram begin precisely where Cepheid stars would be predicted to appear, or a particularly bright RRab Lyrae. There are very few RRab Lyrae stars with magnitudes brighter than ∼-2 in Figure 3, though.

The Lomb-Scargle script gives a period of 5.24 days, which is a fairly long period for an RRab Lyrae star - typically, their periods are up to 1.0 day [Soszynski and OGLE Team, 2020a]. The period agrees with the period outputted by the PDM script [Cullen, 2021]. Cepheids expect their periods to be in the order of 'days'. More data would make it possible to reliably classify this object. Currently, evidence - namely the period and location on the HR-Diagram, favours the Cepheid classification. The GAIA Catalog returns a distance from Gaia EDR3 for this object of 5.5kpc, using [Green et al., 2019] this give an Extinction, E(g-r) value of $0.66^{+0.04}_{-0.01}$. Inputting the 5.24 day period, given by the LombScargle script, the PL relation outputs a magnitude of ∼-3.63. This is within a magnitude of the -3.0 absolute magnitude on the HR-Diagram, supporting the classification of the star as a Cepheid variable.
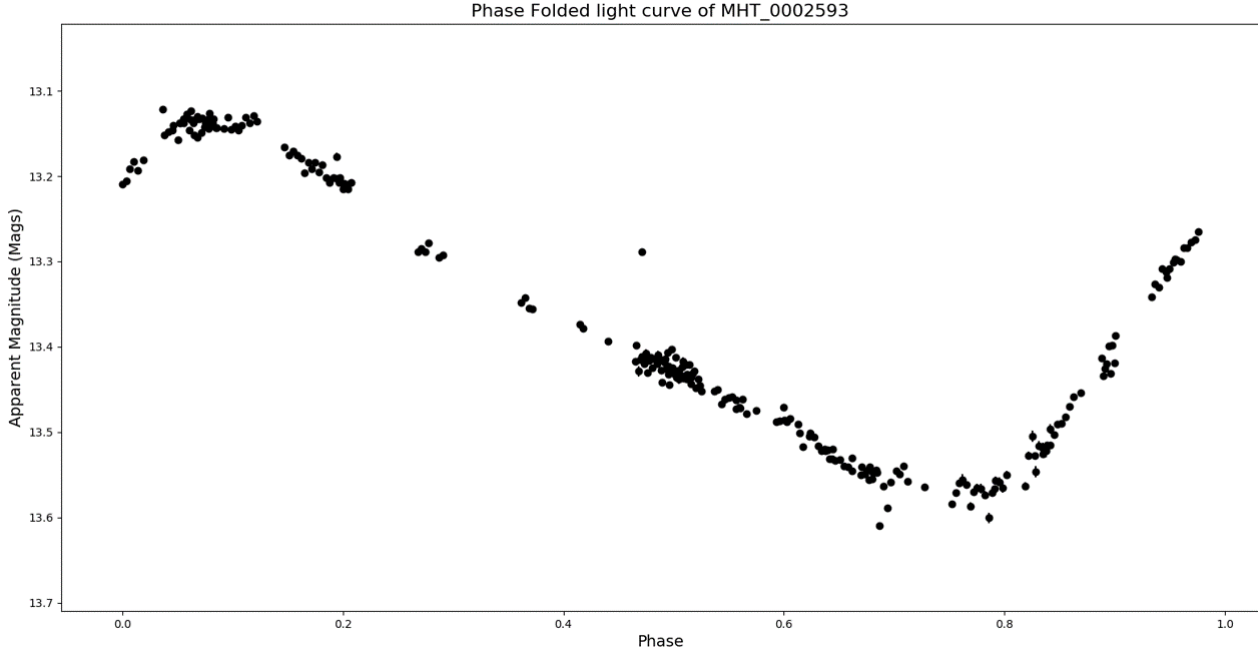
Figure 28: Phase folded light curve of MHT_0002593, with a period of 5.24 days, colour of BP-RP =~1.0 magnitude and an absolute magnitude of ~-3.0 magnitudes.

5.5.2 MHT_0003565

MHT_0003565 lies on the Main sequence in Figure 27. Since we are only looking at objects with a high standard deviation ($>7\sigma$), this narrows down potential classifications to only a few. Of those few, only Eclipsing Binary systems typically lie on the main sequence. From position on the HR-Diagram, at BP-RP=~0.6 magnitudes, and M_G=~0.5 magnitudes, we can make an assumption that the light curve should reinforce the classification as an Eclipsing Binary system. The LombScargle script outputs a period of 1.66 days, which is in agreement with the period output from the PDM script [Cullen, 2021]. Figure 29 shows the light curve for MHT_0003565.

The two different minima suggest the object must be an Eclipsing Binary. The maxima appear to be at different values of apparent magnitude, though - with the first appearing to be at ~15.44 magnitudes, and the second at ~15.49 magnitudes. This is the O'Connell effect [Wilsey and Beaky, 2009], and commonly appears in contact, or near contact binary systems with short periods. The shallower of the two minima has its dimmest magnitude at ~15.75 magnitudes, and the deeper of the two has its dimmest magnitude at ~15.80 magnitudes. There are no flat parts of the light curve, so variation is constant, and the small amplitude of variability suggests the system is more likely to be a W UMa-type Eclipsing Binary.

Figure 29: Phase folded light curve of MHT_0003565, with a period of 1.66 days, colour of BP-RP =∼0.6 magnitudes and an absolute magnitude of ∼0.5 magnitudes.

5.5.3 MHT_0005971

MHT_0005971 lies on the Main Sequence in Figure 27, at BP-RP=∼0.0 magnitudes, and M_G=∼1.5. Similar to MHT_0003565, we would expect to see the typical light curve of an Eclipsing Binary system. The light curve for MHT_0005971, as seen in Figure 30, does not support that classification. The light curve shows a near constant apparent magnitude, at ∼15.75 magnitudes, with one anomalous outlier at ∼16.55 magnitudes. It is likely that the object is not variable, and the anomalous point is a result of an error in the photometry. Comparatively, Figure 31 shows the light curve for MHT_0005971 once the anomaly is removed. There is some variation within the magnitude, but it remains near constant around ∼15.75, and would otherwise not have been detected as a variable in the identification script. This could be an objective for a future project, to improve the identification script so that it is capable of identifying, and removing these outliers. Currently, ∼9% of the 7σ variables fall into this group.
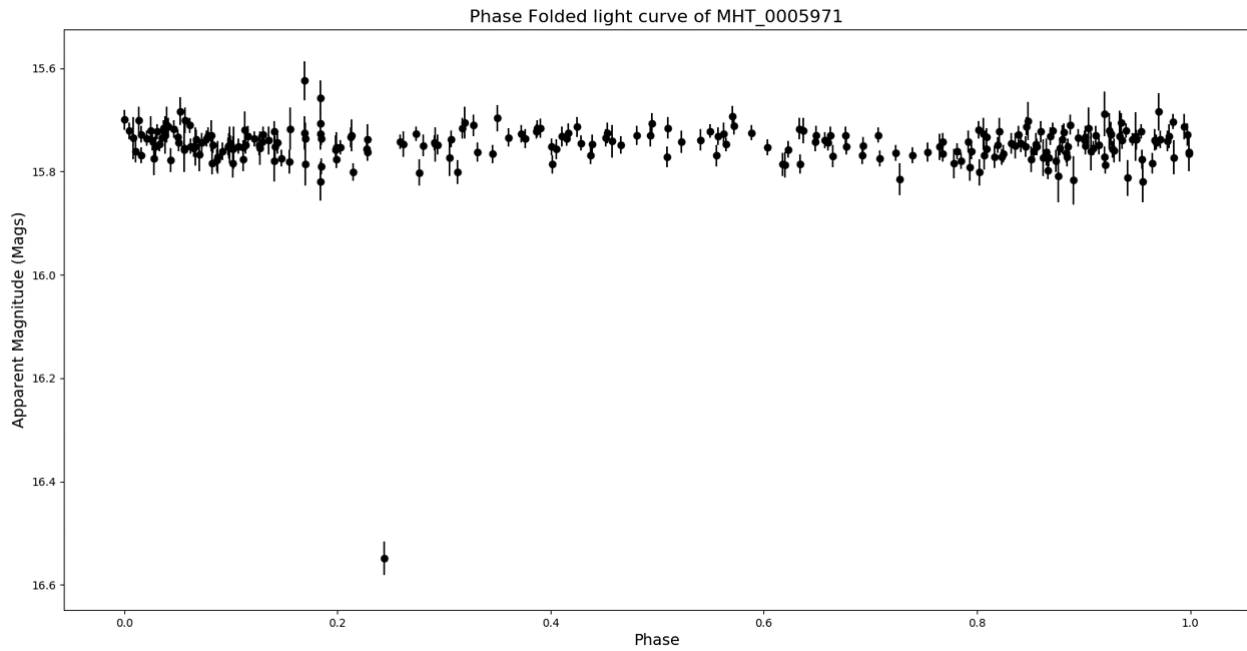
Figure 30: Phase folded light curve of MHT_0005971, with a colour of BP-RP =∼0.0 magnitudes and an absolute magnitude of ∼-1.5 magnitudes.
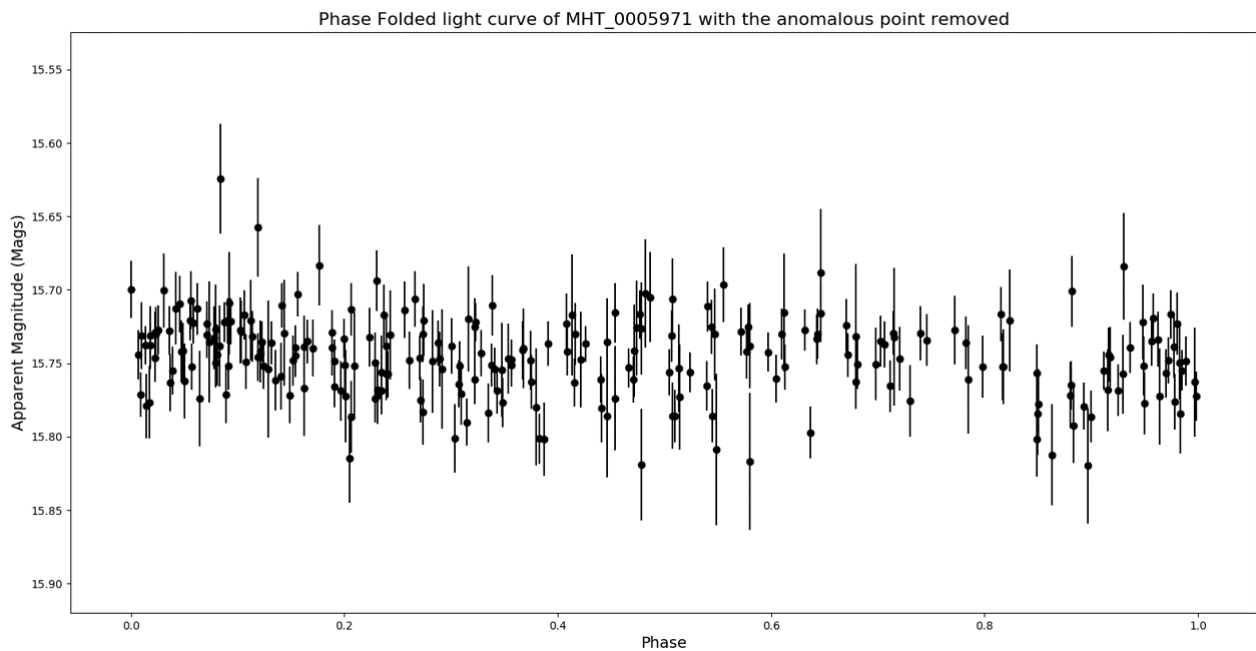
Figure 31: Phase folded light curve of MHT_0005971 with the anomalous point removed.

5.5.4 MHT_0013018

MHT_0013018 lies in the Red Giant Branch in Figure 27. It is at BP-RP=∼3.4 mags, and M_G=∼-1.0, and so according to Figure 3 we only expect to find LPVs in this region of the HR-Diagram. The Lomb-Scargle script returns a period of 255.70 days, supporting the classification as an LPV. The light curve in Figure 32 shows the curve, which has a roughly sinusoidal shape and varies by ∼0.5 magnitudes between ∼13.3 magnitudes and ∼13.8 magnitudes. Sinusoidal

shapes are characteristic of light curves for Mira Type variables, and the small variation in magnitude could support either classification, as semiregular variables typically have V-band variations <2.5 magnitudes [Berlioz-Arthaud, 2016]. Mira type stars have a range of amplitudes, but commonly vary by up to 8 magnitudes in visual wavelengths [Reid and Goldston, 2002]. The curve does not suggest multiperiodicity, however, which is a common trait in the semiregular variable stars [Kiss et al., 1999].
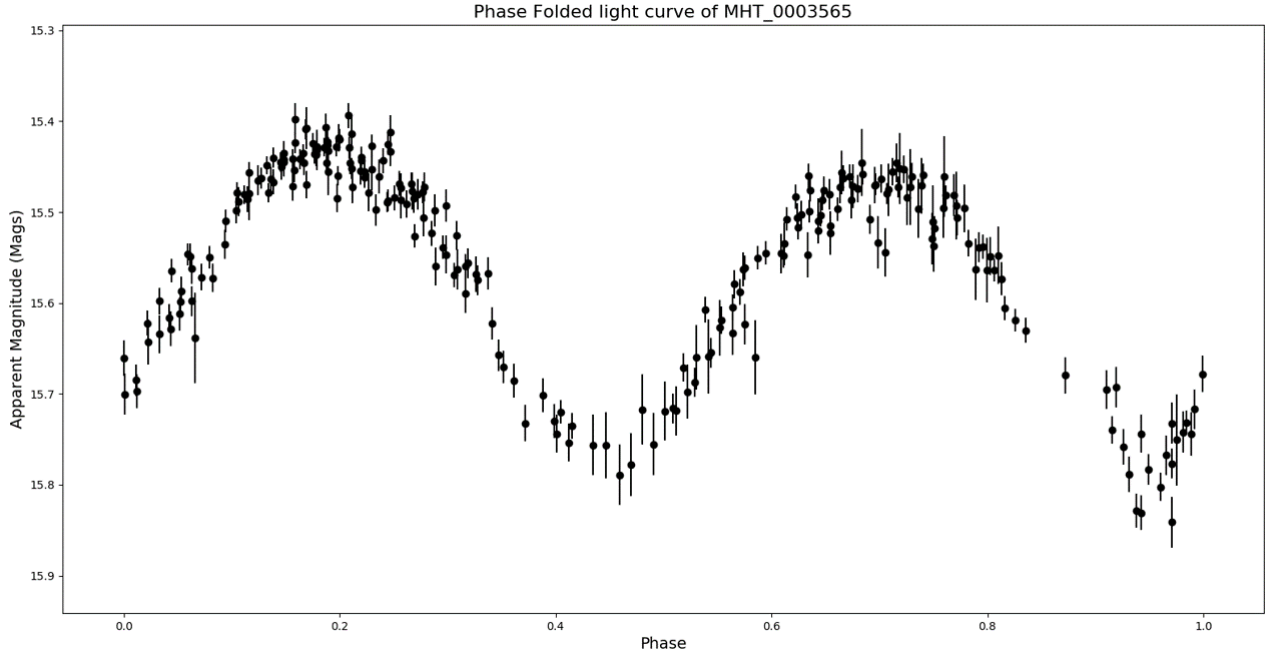

Figure 32: Phase folded light curve of MHT_000013018, with a period of 255.70 days, colour of BP-RP =∼3.4 magnitudes and an absolute magnitude of ∼-1.0 magnitudes.

5.5.5   MHT_0015257

MHT_0015257 lies on the Main Sequence. We would not expect an object lying on the Main Sequence, and displaying such high standard deviation in magnitude, to have the expected light curve of a Mira type star, or a Classical Cepheid, but an eclipsing binary system. The Light Curve in Figure 33 displays the sinusoidal shape expected of a W UMa-type eclipsing binary, as seen in the bottom panel of Figure 12. The maxima lie at ∼11.76 magnitudes, and the two minima are different. The deeper of the two is ∼12.14 magnitudes, a depth of ∼0.38 magnitudes. The shallower is ∼12.10, a depth of ∼0.34 magnitudes. The difference in variation for the minimum is 0.04 magnitudes, a small difference like this suggests the stars are similar in size. The LombScargle script gives a period of 0.51 days (∼12.24 hours) - short periods are expected of W UMa-type light curves. The shape of the curve, showing constant variation with very little time spent at the maximum magnitude, is also characteristic of a W UMa curve, largely due to the small orbital radii the systems often have. The shape of the curve, period, and position on the HR-Diagram all support the classification of MHT_0015257 as a W UMa Eclipsing Binary System.

Figure 33: Phase folded light curve of MHT_0015257, with a period of 0.51 days, colour of BP-RP =~0.4 magnitudes and an absolute magnitude of ~2.5 magnitudes.

5.5.6 MHT_0015992

MHT_0015992 lies on the Red giant branch of Figure 27, with a BP-RP of ~2.5 mags and an absolute magnitude of ~-2.0 magnitudes. Based on figure 3, it lies in the region where we would expect to identify LPVs, Cepheid variables and potentially RV Tauri stars. The Lomb-Scargle script returns a value of 123.54 days for the object's period. Typically, Cepheid variables have periods within the region of days, but the period could suggest either classification, as RV Tauri stars' periods can reach up to 150 days [Gezer et al., 2015] and Gaia EDR3 defines LPVs as having periods > 60 days [Gaia Collaboration, 2021]. The light curve in Figure 34 seems to have a steep decline, and a shallow incline, varying between ~14.25 magnitudes and ~14.5 magnitudes. Mira type LPVs often have sinusoidal light curves, such as in Figure 9. Figure 34 displays multiple periods, which could be taken as a sign that the star is of the RV Tauri classification or a Semiregular variable.

RVb Tauri stars have two light curves, one folded over a long period, and the second curve that is equivalent to an RVa Star. Multiperiodicity is also a sign that the object could be a semiregular variable. The ~0.25 magnitude variation can also be an indicator of either RV Tauri classification, which can have variations of up to 4 magnitudes [Gezer et al., 2015]. Semiregular variations have smaller magnitudes, up to 2.5 magnitudes in the V-band, The introduction of more data to the MOSES data set could help classify the object. There were 72 semiregular variables with multiple periods identified in the All Sky Automated Survey (ASAS) [Fuentes-Morales and Vogt, 2014]. Introducing external data may help to 'fill in the gaps' in the light curve, and allow for a more accurate classification.
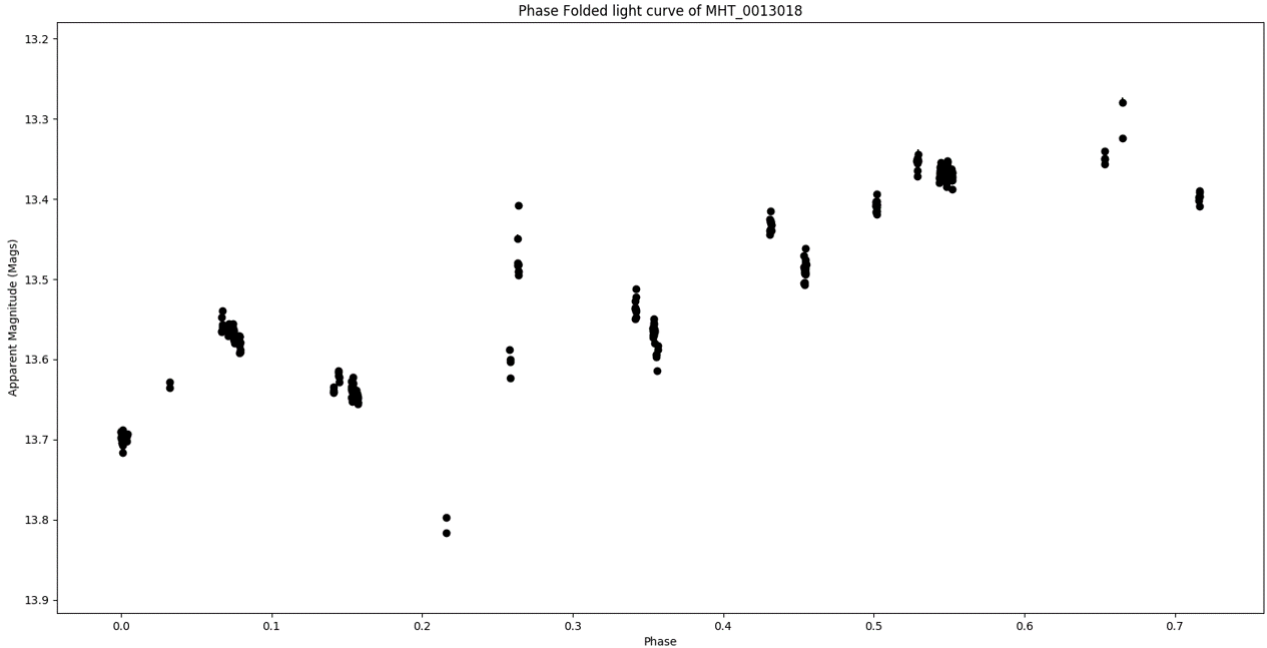
Figure 34: Phase folded light curve of MHT_0015992, with a period of 123.54 days, colour of BP-RP =∼2.5 magnitudes and an absolute magnitude of ∼-2.0 magnitudes.

5.5.7 MHT_0019577

MHT_0019577 lies on the Main Sequence of Figure 27. It is one of the stars in the sample of least variable stars taken to check that the variable stars discovered by this iteration of the survey, but not by the first, are variable. It varies by ∼0.05 magnitudes, between ∼13.55 magnitudes and ∼13.50 magnitudes. The Lomb Scargle script returns a period of 0.15 days. Its position on the HR-Diagram suggests it is most likely an Eclipsing Binary system, though such a short period suggests the system has a very short orbital radius. The Light Curve in Figure 35 shows two minima, supporting this. There is not much difference in the magnitude of the minimum, both are at ∼13.55 magnitudes, but the second maximum appears greater than the first, albeit only by ∼0.01 magnitudes. There is constant variation in the curve, suggesting it is a W UMa type Eclipsing Binary system, but classification of the object would benefit from more observations due to its low σvalue.
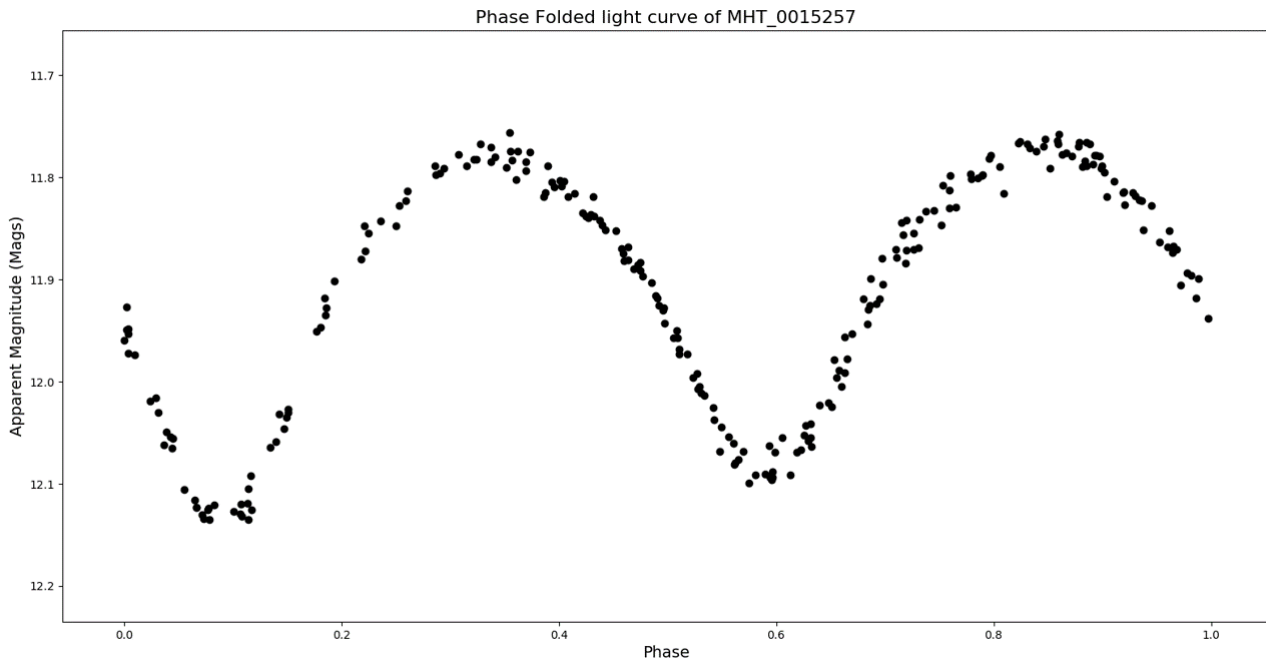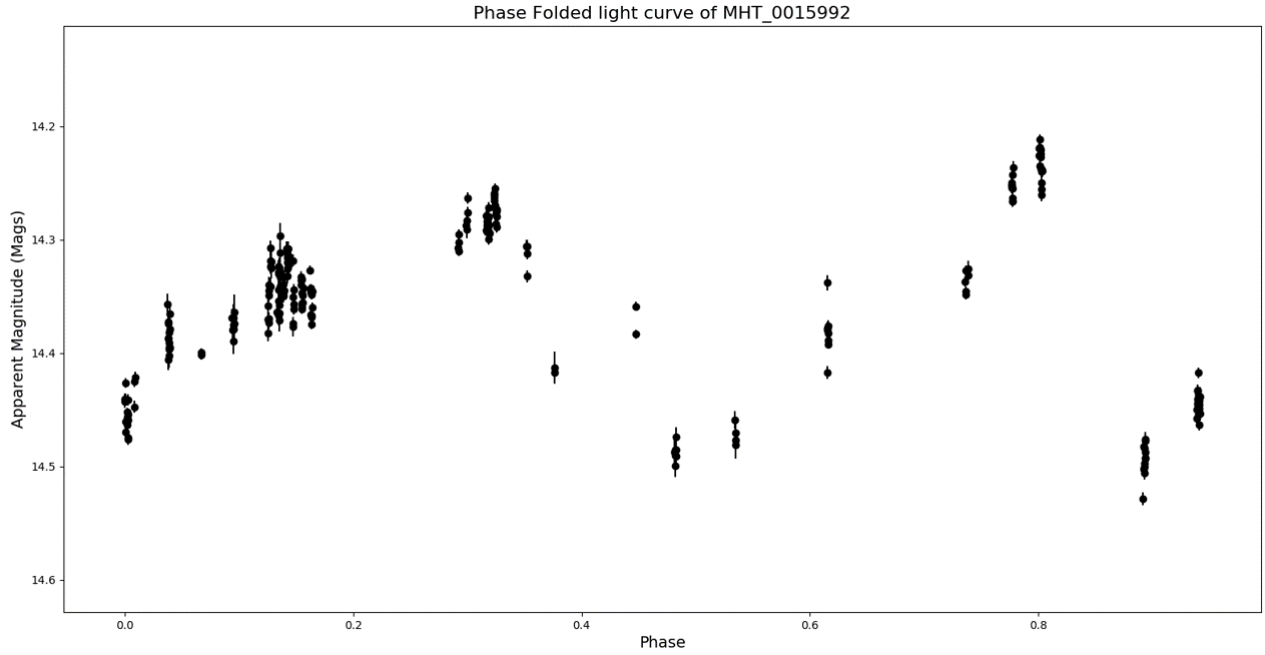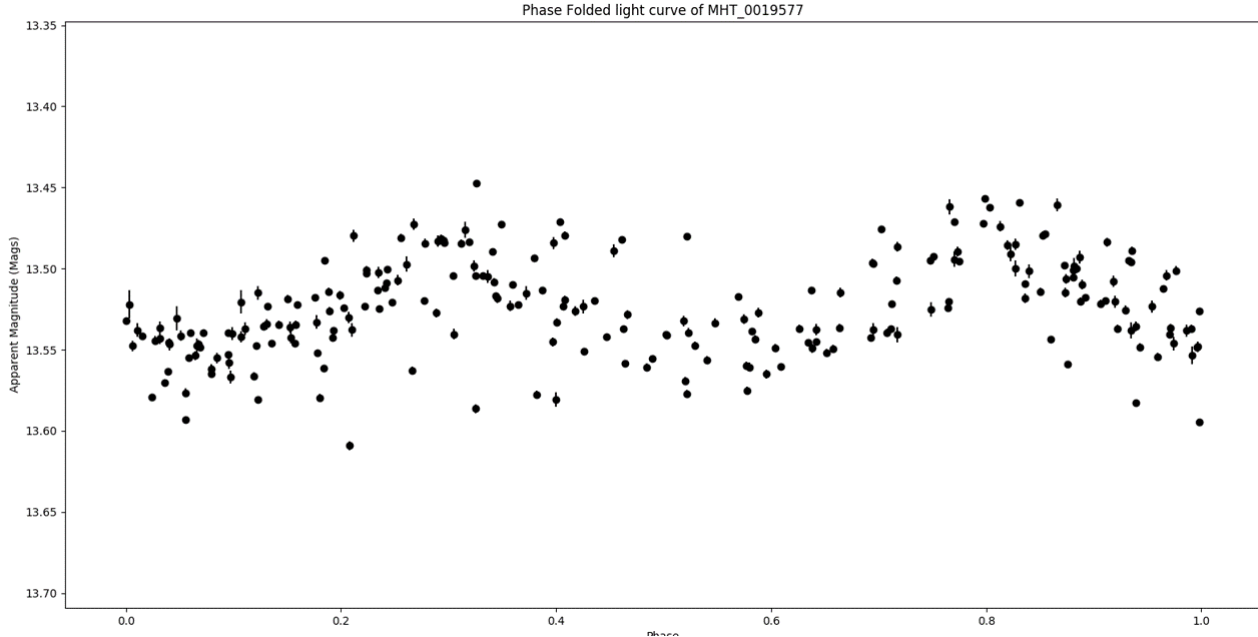
Figure 35: Phase folded light curve of MHT_0019577, with a period of 0.15 days, colour of BP-RP =∼0.5 magnitudes and an absolute magnitude of ∼2.0 magnitudes.

5.6 MOSES Survey Flowchart

The following flowchart in Figure 36 shows the basic, step-by-step process that future iterations of the MOSES Survey could follow to classify all ∼100,000 observed objects. Once the images are obtained, they are to be reduced using the improved reduction pipeline, eliminating the need to obtain flatfield images on, or around, the night of observation. The WCS-fixing script should also be used on the images once they're reduced, ensuring the ability to coadd the images. The next step would be to run the images through the catalog creation pipeline. This will return the .csv files for each object, and then write the *Master Catalog* containing the basic information, such as the name, positional data, median magnitude, standard deviation, and number of observations. This Master Catalog can then be run through the Variable Identification script, which will highlight variables above 3σ standard deviations in their magnitude, highlighting the variables in groups as shown in Figure 27, where the '>7σ' group is highlighted. The script will also write these variables into smaller catalogs. Future improvements should remove outliers in the light curves that falsely inflate the σ of individual stars, resulting in false positives being included in the catalogs of variables.

During this project, the highlighted groups and smaller catalogs contained objects with greater than 3σ objects with greater than 5σ and objects with greater than 7σ. The csv files for objects confirmed to be variable can then be run through the Lomb Scargle script, or another light curve plotting script, such as the PDM script by [Cullen, 2021]. This will provide phase folded light curves and, in the case of the script a period in days. The shape of the light curve, period, and amplitude of variation can be compared with literature values in order to determine a first, basic classification. This classification can be verified by running the catalog of all variable stars through the HR-Diagram script, highlighting the objects that are currently being analysed. Figure 3 shows the various areas variable stars can lie in on the HR-Diagram, so once plotted, the star's classification can be narrowed down to fewer classes. If the classification suggested by the light curve is in agreement with a class suggested by position on the HR-Diagram, then the

star can be classified by the MOSES Survey. The classification can also then be compared to literature values, as the object may have been classified by other surveys, such as TESS or the ZTF. If they do not agree, these steps can be repeated in case there is any error, and further investigation into why the two do not agree should be performed.

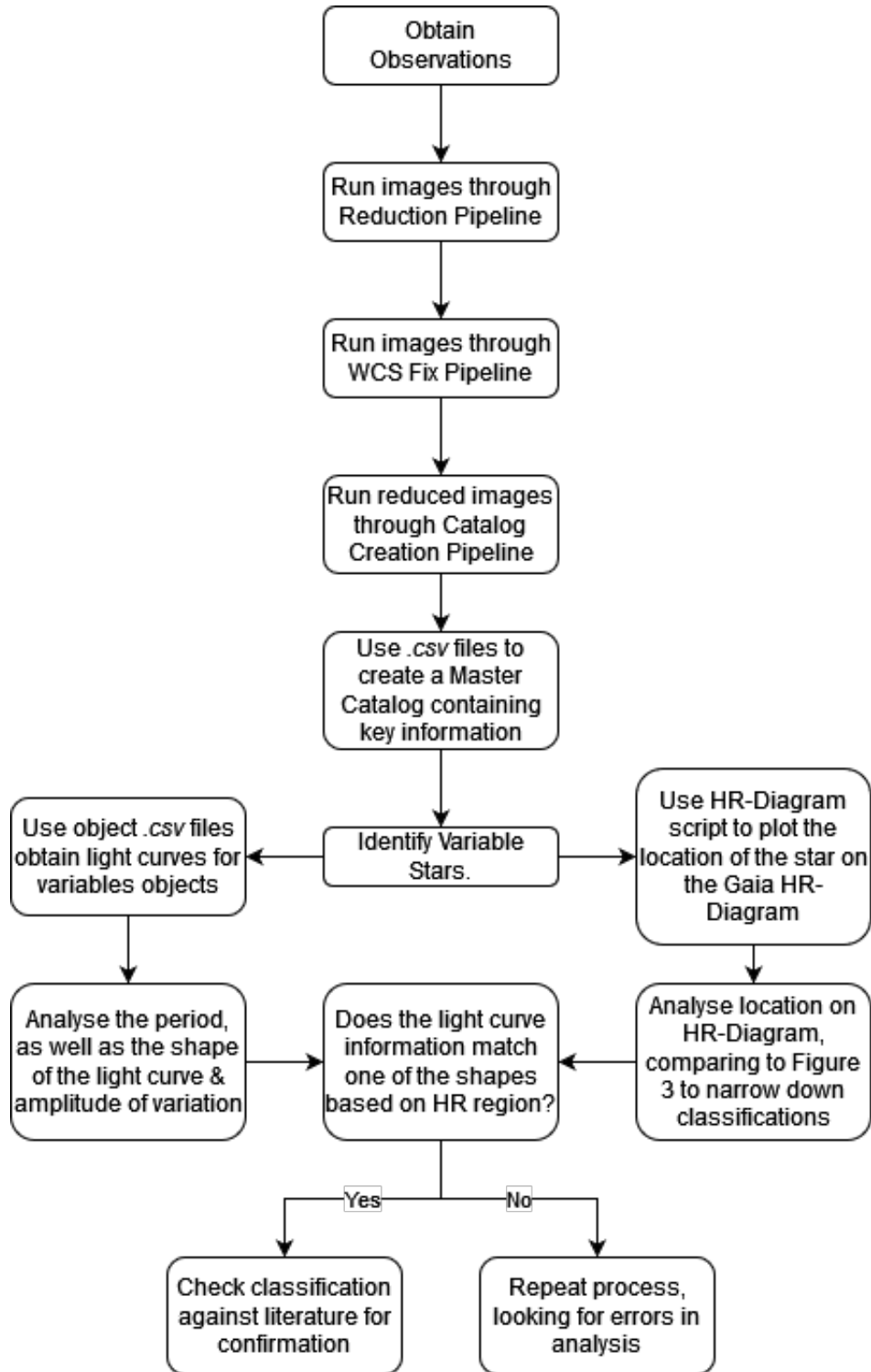**Figure 36:** Basic Flowchart to be followed in future iterations of the MOSES Survey.

6   Discussion

This project did not manage to complete the objective it had initially intended. The collection of new data, increasing the baseline for the survey, was prevented by the damage to the dome and the ongoing COVID-19 pandemic. Analysis, and classification of the variable stars discovered, was also not performed to the level initially intended due primarily to time constraints as it took longer than initially anticipated to get many of the scripts running on the various computer systems, a consequence of remote working. Despite that, the survey has been enhanced by the work performed in this thesis, and this project has made use of extra information that was unavailable to [Rambukwella-Gill, 2019] in the previous iteration, such as the Gaia EDR3 data. We have enhanced the reduction process, improving the photometry, as shown in Figure 22, reducing the amount of false variables detected. We also improved upon the treatment of the WCS, allowing future iterations of the survey to coadd images, potentially identifying fainter objects in the field. Future projects will not have to revise the reduction process, and can focus on further observations and in depth analysis.

We have defined what we consider to be a variable star within the MOSES data ($>3\sigma$) and identified 1495 variable objects in the dataset, though some false detections remain ($\sim10\%$). This is slightly more than double the 719 variable objects in the first iteration of the project [Rambukwella-Gill, 2019]. The project made use of Gaia EDR3 to plot the objects on a HR-Diagram, and further reinforce the classification of the object once the light curve and period have been obtained. The methods utilised to identify variables, and to classify them, are applicable to future iterations of the MOSES Survey once data has been obtained. It is extremely likely that there are variable stars that have not been identified as variable by the project because their variation in magnitude was too small relative to our current number of observations and photometric noise floor. Making use of external data sets has the potential to help identify these objects. Adding data from external sources such as TESS, the ZTF, and All-Sky Automated Survey for Supernovae (ASAS-SN) to MOSES would increase the baseline, and allow for more objects to be identified within the field, though complications exist due to the differences in filter systems used.

Future projects at both an MSc and BSc level can make use of the improved data set, and access to Gaia in the creation of the HR-Diagram. In depth analysis can be performed on the data at the groupings of -sigma defined earlier in section 5.2 to attempt to classify each star. The projects performing in depth analysis can make use of other, larger data sets similar to our use of the Gaia EDR3 release, such as TESS data, which would extend the survey's baseline, or data from the ZTF, where the shorter baseline would serve to 'fill in the gaps' for the MOSES survey. The extra datasets would improve upon the MOSES data by providing more observations of an object than MOSES alone.

An interesting future project is the automation of the classification process, using a training set of data. A portion of the data, ($\sim25\%$, for example) can be classified manually using the classification tree in Figure 1 and the Flowchart in Figure 35. If enough objects are classified this way, and there is a good distribution of data in each classification, the information used to classify stars can then be used for the basis of a machine learning project that would automate the process. Once the periods had been obtained, the machine learning script would make use of the scripts in this project to identify variable stars, and to obtain values for the magnitude of the object and magnitude of variability, the object's light curve and the object's position on the

HR-Diagram. It would use the previously classified stars to identify what parameters would be used to classify an object. For example, to classify an object as a Cepheid variable, it would look for the sawtooth shape to the curve, position in the instability strip or red giant branch, and would then attach the 'Cepheid' label to the object. This would then be checked against known literature to ensure the result is correct. For a machine project to work, there must be a good spread of the objects that are classified manually, as the script would need enough examples in each classification to identify the parameters in the objects it attempts to classify.

7 Conclusion

In this paper, I have outlined the enhancements made to the MOSES Survey initiated by [Rambukwella-Gill, 2019]. The improved photometry has identified 98,580 objects within the field, of which 1495 were confirmed as variable (despite using a more restricted magnitude range) using the 3σ method implemented. This is an increase from 87,397 objects, of which 719 were variable, in the first iteration of the survey [Rambukwella-Gill, 2019]. The difference is due to the improved flatfielding allowing us to find more objects, and the improved method with which we calculated 3σ above which objects are deemed variable. It is unfortunate that the project was unable to extend the survey by collecting more observations, but improvements made have ensured future projects are able to focus on extending the survey and performing analysis on the data.

A second, complete observing season's worth of data will allow the periods of confirmed variables to be calculated with increased accuracy, as more periods of each object will have been observed. The detection of Long Period Variables will also significantly improve with more observations, currently there are 28 nights worth of observations taken over the course of a year [Rambukwella-Gill, 2019]. LPVs are defined as having periods greater than 60 days [Gaia Collaboration, 2021]. More observations would help 'fill in the gaps' in the light curves of the LPVs, improving the accuracy of the subclassifications given to them, such as Mira type, or Semiregular.

Projects are already making use of the MOSES Data, such as [Cullen, 2021]. [Cullen, 2021] has taken the data from the first iteration of the survey, and used it to identify Eclipsing Binary systems within the field. 70 were identified by her project. It would be interesting to see a comparison of the results from her project using both the old, and improved photometry. The improvements made resulted in more than double the amount of stars being identified as variable, so we would also expect a corresponding increase in Eclipsing Binaries identified. Similar projects could be undertaken at both an undergraduate and postgraduate level, focusing on a specific classification of star and using the methods outlined in this project to identify those objects within the MOSES data. Eventually, one such project has the potential to identify transiting exoplanets in the survey field too.

References

Anderson, R. T., Ekström, S., Georgy, C., Meynet, G., and Saio, H. (2017). How rotation affects masses and ages of classical Cepheids. *EPJ Web of Conferences.* http://dx.doi.org/10.1051/epjconf/201715206002 [Accessed: 10-September-2021].

ANDOR (2019). Apogee Aspen CG16M. https://andor.oxinst.com/assets/uploads/documents/Andor/apog

Australia Telescope National Facility (2018). Classification tree of variable stars. Master's thesis.

Bellm, E. C., Kulkarni, S. R., Graham, M. J., Dekany, R., Smith, R. M., Riddle, R., Masci, F. J., Helou, G., Prince, T. A., and Adams, S. M. (2018). The Zwicky Transient Facility: System Overview, Performance, and First Results. *Publications of the Astronomical Society of the Pacific*, 131(995). https://iopscience.iop.org/article/10.1088/1538-3873/aaecbe.

Berlioz-Arthaud, P. (2016). Long Period Variables: questioning the pulsation paradigm. https://arxiv.org/abs/1608.00232 [Accessed: 11-September-2021].

Bertin, E. and Arnouts, S. (1995). SExtractor: Software for source extraction. *Astronomy and Astrophysics Supplement*, 117:393 – 404. https://ui.adsabs.harvard.edu/link_gateway/1996A&AS..117..393B/doi:10.1051/aas:1996164 [Accessed: 27-August-2021].

Bertin, E. and Arnouts, S. (1996). SExtractor: Software for source extraction. A&AS, 117:393–404. https://ui.adsabs.harvard.edu/abs/1996A&AS..117..393B.

Bertin, E. and Marmo, C. (2021). Astromatic.net. https://www.astromatic.net/about/ [Accessed: 29-August-2021].

Bertin, E., Mellier, Y., Radovich, M., Missonnier, G., Didelon, P., and Morin, B. (2002). The TERAPIX Pipeline. *Astronomical Data Analysis Software and Systems XI*, 281:228. http://adsabs.harvard.edu/pdf/2002ASPC..281..228B [Accessed: 28-August-2021].

Bono, G., Caputo, F., and Santolamazza, P. (1997). Evolutionary scenario for metal-poor pulsating stars. I. Type II Cepheids. *Astronomy and Astrophysics*, 317:171 – 177. https://ui.adsabs.harvard.edu/abs/1997A%26A...317..171B/abstract [Accessed: 15-September-2021].

Calabretta, M. R. and Greisen, E. W. (2002). Representations of celestial coordinates in FITS. *Astronomy and Astrophysics*, 395:1077 – 1122. https://www.atnf.csiro.au/people/mcalabre/WCS/ccs.pdf [Accessed: 28-August-2021].

Casagrande, L. and VandenBerg, D. A. (2018). On the use of Gaia magnitudes and new tables of bolometric corrections. *Monthly Notices of the Royal Astronomical Society: Letters*, 479(1):L102 – L107. https://arxiv.org/abs/1806.01953 [Accessed: 31-August-2021].

Cullen, J. (2021). Identifying and Characterising Eclipsing Binary Stars in the MOSES Survey. Master's thesis, University of Central Lancashire. No URL currently available.

Dambis, A. K., Berdnikov, L. N., Kniazev, A. Y., Kravstov, V. V., Rastorguev, A. S., Sefako, R., and Vozyakova, O. V. (2013). RR Lyrae Variables: visual and infrared luminosities, intrinsic colours and kinematics. *Monthly Notices of the Royal Astronomical Society*, 435(4):3206 – 3220.

Fuentes-Morales, I. and Vogt, N. (2014). Multiperiodic semiregular variable stars in the ASAS data base: A pilot study. *Astronomische Nachrichten*, 335(10):1072 – 1077. http://dx.doi.org/10.1002/asna.201412117 [Accessed: 18-September-2021].

Gaia Collaboration (2021). Gaia Early Data Release 3. *Astronomy & Astrophysics*, 649. https://doi.org/10.1051/0004-6361/202039657 [Accessed: 15-September-2021].

Gezer, I., Van Winckel, H., Bozkurt, Z., De Smedt, K., Kamath, D., Hillen, M., and Manick, R. (2015). The WISE view of RV Tauri Stars. *Astronomical Society of the Pacific Conference Series*, 497:223.

Gillion et al. and ESO/M. (2017). Light Curves of the seven TRAPPIST-1 planets as they transit. https://www.eso.org/public/images/eso1706h/ [Accessed: 18-August-2021].

Good, G. A. (2003). Rotating Variable Stars. *Observing Variable Stars, Patrick Moore's Practical Astronomy Series*. https://link.springer.com/chapter/10.1007/978-1-4471-0055-3_6#citeas [Accessed: 30-August-2021].

Green, G. M. (2018). dustmaps: A Python interface for maps of interstellar dust. *The Journal of Open Source Software*, 3(26):695. https://ui.adsabs.harvard.edu/abs/2018JOSS....3..695G/abstract [Accessed: 31-August-2021].

Green, G. M., Schlafly, E., Zucker, C., Speagle, J. S., and Finkbeiner, D. (2019). A 3D Dust Map Based on Gaia, Pan-STARRS 1, and 2MASS. *The Astrophysical Journal*, 887(1):93. http://dx.doi.org/10.3847/1538-4357/ab5362 [Accessed: 17-September-2021].

Groenewegen, M. A. T. (2018). The Cepheid period-luminosity-metallicity relation based on Gaia DR2 data. *Astronomy & Astrophysics*, 619. https://ui.adsabs.harvard.edu/abs/2018A&A...619A...8G [Accessed: 16-September-2021].

Hameury, J.-M. (2020). A review of the disc instability model for dwarf novae, soft X-ray transients and related objects. *Advanced in Space Research*, 66(5):1004 – 1024. http://dx.doi.org/10.1016/j.asr.2019.10.022 [Accessed: 13-September-2021].

Hameury, J. M. and Lasota, J. P. (2005). Classical Nova Explosions. *The Astrophysics of Cataclysmic Variables and Related Objects: ASP Conference Series*, 330.

Hummerich, S., Bernhard, K., and Srdoc, G. (2013). Twenty New W Ursae Majoris-type Eclipsing Binaries. 5. https://vs-compas.belastro.net/bulletin/issue/2/p6 [Accessed: 04-August-2021].

Joy, A. H. (1937). Radial Velocities of Cepheid Variable Stars. *Astrophysical Journal*, 8:363.

Kantharia, Nimisha G. (2017). Novae: I. The maximum magnitude relation with decline time (MMRD) and distance. https://arxiv.org/pdf/1703.04087.pdf [Accessed: 30-August-2021].

Karttunen, H., Oja, H., Poutanen, M., Donner, K. J., and Kröger, P. (2016). *Fundamental Astronomy*. Springer Berlin / Heidelberg, Berlin, Heidelberg.

Kiss, L. L. and Bodi, A. (2017). Amplitude variations of modulated RV Tauri stars support the dust obscuration model of the RVb phenomenon. *Astronomy & Astrophysics*, 608. https://doi.org/10.1051/0004-6361/201731876 [Accessed: 10-July-2021].

Kiss, L. L., Szatmary, K., Cadmus Jr., R. R., and Mattei, J. A. (1999). Multiperiodicity in semiregular variables - I. General properties. https://arxiv.org/pdf/astro-ph/9904128.pdf [Accessed: 13-July-2021].

Leavitt, H. S. and Pickering, E. C. (1912). Periods of 25 Variable Stars in the Small Magellanic Cloud. *Harvard College Observatory Circular*, 173:1–3.

Majaess, D. J., Turner, D. G., and Lane, D. J. (2009). Type II Cepheids as Extragalactic Distance Candles. *Acta Astronomica*, 59(4):403 – 418.

Mattei, J. A. (1996). Introducing Mira Variables. *The American Association of Variable Star Observations*, 25(2).

MaxIm DL (2021). MaxIm DL User Manual. https://cdn.diffractionlimited.com/help/maximdl/MaxIm-DL.htm [Accessed: 04-January-2022].

Muller, G. and Kempf, P. (1903). A new variable star of unusually short period. *Astrophysical Journal*, 17. https://ui.adsabs.harvard.edu/abs/1903ApJ....17..201M/abstract [Accessed: 17-August-2021].

Percy, J. R. (2007a). *Understanding Variable Stars*. Cambridge University Press. DOI: https://doi.org/10.1017/CBO9780511536489.

Percy, J. R. (2007b). Understanding Variable Stars. http://cfas.org/data/uploads/astronomy-ebooks/variable-stars.pdf [Accessed: 31-August-2021].

Rambukwella-Gill, A. (2019). MOSES: MHT Optical Star and Exoplanet Survey. Master's thesis, University of Central Lancashire. http://clok.uclan.ac.uk/34495/.

Reid, M. J. and Goldston, J. E. (2002). How Mira Variables Change Visual Light by a Thousandfold. *The Astrophysical Journal*, 568(2):931 – 938. http://dx.doi.org/10.1086/338947 [Accessed: 16-September-2021].

Shafter, A. W. (2017). The Galactic Nova Rate Revisited. *The Astrophysical Journal*, 834(2). https://iopscience.iop.org/article/10.3847/1538-4357/834/2/196 [Accessed: 28-August-2021].

Singh, M., Misra, K., Sahu, D. K., Dastidar, R., Gangopadhyay, A., Srivastav, S., Anupama, G. C., Bose, S., Lipunov, V., Chakradhari, N. K., Kumar, B., Kumar, B., Pandey, S. B., Gorbovskoy, E., and Balanutsa, P. (2019). Observational properties of a Type Ib Supernova. https://arxiv.org/pdf/1903.06243.pdf [Accessed: 27-July-2021].

Soszynski, I. and OGLE Team (2020a). OGLA Atlas of Variable Star Light Curves: RR Lyrae Stars. http://ogle.astrouw.edu.pl/atlas/RR_Lyr.html [Accessed: 08-July-2021].

Soszynski, I. and OGLE Team (2020b). OGLA Atlas of Variable Star Light Curves: RV Tauri Stars. http://ogle.astrouw.edu.pl/atlas/RV_Tau.html [Accessed: 10-July-2021].

Soszynski, I. and OGLE Team (2020c). RV Tauri Stars. http://ogle.astrouw.edu.pl/atlas/RV_Tau.html [Accessed: 12-July-2021].

Soszynski, I., Udalski, A., Wrona, M., Szymanski, M. K., Pietrukowicz, P., Skowron, J., Skowron, D., Poleski, R., Kozlowski, S., Mroz, P., Ulaczyk, K., Rybicki, K., Iwanek, P., and Gromadski, M. (2019). Over 78 000 RR Lyrae stars in the Galactic Bulge and Disk from the OGLE Survey. *Acta Astronomica*, 69:312 – 337.

Swinburne University of Technology (2021a). Classical Novae. https://astronomy.swin.edu.au/cosmos/C/Classical+Novae [Accessed: 20-August-2021].

Swinburne University of Technology (2021b). Recurrent Novae. https://astronomy.swin.edu.au/cosmos/R/Recurrent+Novae [Accessed: 20-August-2021].

Swinburne University of Technology (2021c). Roche Lobe. https://astronomy.swin.edu.au/cosmos/r/roche-lobe [Accessed: 16-August-2021].

Swinburne University of Technology (2021d). Supernova Classification. https://astronomy.swin.edu.au/cosmos/s/supernova+classification [Accessed: 20-August-2021].

Swinburne University of Technology (2021e). Type Ia Supernova Light Curves. https://astronomy.swin.edu.au/cosmos/T/Type+Ia+supernova+light+curves [Accessed: 17-July-2021].

Tanvir, N. R., Hendry, M. A., Watkins, A., Kanbur, S. M., Berdnikov, L. N., and Ngeow, C. C. (2005). Determination of Cepheid Parameters by light-curve template fitting. *Monthly Notices of the Royal Astronomical Society*, 363(3):749 – 762.

TESS Team (2014). Transiting Exoplanet Survey Satellite. *Journal of Astronomical Telescopes, instruments and systems*, 1. https://doi.org/10.1117/1.JATIS.1.1.014003.

University of Central Lancashire (2017). The Moses Holden Telescope at Alston Observatory. http://www.star.uclan.ac.uk/wp-content/uploads/2017/12/PICT6202.jpg [Accessed: 22-December-2021].

VanderPlas, Jacob T. (2018). Understanding the Lomb-Scargle Periodogram. *The Astrophysical Journal Supplement Series*, 236(1):16. https://doi.org/10.3847/1538-4365/aab766 [Accessed: 16-September-2021].

Vink, J. (2017). Supernova 1604, Kepler's supernova, and it's remnant. *Handbook of Supernova*, pages 139 – 160. https://arxiv.org/pdf/1612.06905.pdf [Accessed: 29-August-2021].

Ward-Thompson, Derek and Butchart, Ian (2016). A New Planewave 0.7-metre Telescope for Alston Observatory. http://www.star.uclan.ac.uk/wp-content/uploads/2017/12/alston_poster_1.pdf.

Wilsey, N. J. and Beaky, M. M. (2009). Revisiting the O'Connell Effect in Eclipsing Binary Systems. *Society for Astronomical Sciences Annual Symposium*, 28:107. https://ui.adsabs.harvard.edu/abs/2009SASS...28..107W [Accessed: 19-September-2021].

Wilson, L. A. and Templeton, M. (2019). Miras, RV Tauri Stars, and the Formation of Planetary Nebulae. https://doi.org/10.1063/1.3246421 [Accessed: 12-July-2021].

Woosley, S. E. and Eastman, R. G. (1997). *Type Ib and Ic Supernovae: Models and Spectra.* Springer, Dordrecht, Dordrecht. NATO ASI Series (Series C: Mathematical and Physical Sciences), vol 486. https://doi.org/10.1007/978-94-011-5710-0_51.

Appendix 1.0: Scripts

Figure 37: The Python script utilised to identify variable objec1ts in the data set.

Figure 38: The Python script utilised pair the MOSES Data with the Gaia EDR3 Data [Gaia Collaboration, 2021].

```python
import numpy as np
import matplotlib.pyplot as plt
from gatspy.periodic import LombScargleFast
import pandas as pd

df1 = pd.read_csv('/san/galactic/ldabbs/SummaryPlots/LightCurves/Latest/MHT_0015257/MHT_0015257.csv')
t = df1.JD
mag = df1.Aper_Mag_Zero
dmag = df1.Aper_Mag_Err
model = LombScargleFast().fit(t, mag, dmag)
periods, power = model.periodogram_auto(nyquist_factor=100)

fig, ax = plt.subplots()
ax.plot(periods, power)
ax.set(xlim=(0.0, 300), ylim=(0, 0.8),
       xlabel='period (days)',
       ylabel='Lomb-Scargle Power');
plt.show()

# set range and find period
model.optimizer.period_range=(0.1, 300)
period = model.best_period*2
print("period = {0}".format(period))



phase = ((np.array(t)-np.array(t)[0])/(period)) - np.floor((np.array(t)-np.array(t)[0])/(period))

plt.scatter(phase,mag,color='k',marker='o')
plt.errorbar(phase, mag, yerr = dmag, color='k', fmt='none')
plt.xlabel('Phase', fontsize='14')
plt.ylabel('Apparent Magnitude (Mags)', fontsize='14')
plt.title("Phase Folded light curve of MHT_0015257", fontsize='16')
plt.ylim(max(mag)+0.1,min(mag)-0.1)
plt.show()
```

Figure 39: The Python script utilising Lomb Scargle to produce light curves. In this instance,for MHT_001527